Spatial Tracker for an Air-to-Ground Laser Communication Link

by

William G. Near

Submitted to the Department of Electrical Engineering and Computer Science
in partial fulfillment of the requirements for the degree of

Master of Engineering in Electrical Engineering and Computer Science

at the

MASSACHUSETTS INSTITUTE OF TECHNOLOGY

February 2012

Author .....
Department of Electrical Engineering and Computer Science
February 1, 2012

Certified by .....
James K. Roberge
Professor of Electrical Engineering
Thesis Supervisor

Certified by .....
Robert J. Murphy
MIT LL Group 66, Technical Staff
Thesis Supervisor

Accepted by .....
Prof. Dennis M. Freeman
Masters of Engineering Thesis Committee

Spatial Tracker for an Air-to-Ground Laser Communication Link

by

William G. Near

Submitted to the Department of Electrical Engineering and Computer Science
on February 1, 2012, in partial fulfillment of the
requirements for the degree of
Master of Engineering in Electrical Engineering and Computer Science

Abstract

In this thesis, I designed several of the hardware components of a spatial tracker for an air-to-ground laser communication system; these include a PWM switching amplifier and the control systems for driving the primary steering and tracking elements required in the acquisition and maintenance of an optical communication link. The hardware was designed for low size, weight, and power (SWaP), low cost, and easy system integration. A performance analysis is presented comparing the designed hardware to a benchmark lasercom system developed at MIT Lincoln Laboratory.

Thesis Supervisor: James K. Roberge
Title: Professor of Electrical Engineering

Thesis Supervisor: Robert J. Murphy
Title: MITLL Group 66, Technical Staff

Acknowledgments

I would like to thank a number of people who have been instrumental in the completion of my master's thesis. First, I would like to thank my direct supervisor Robert Murphy, who welcomed me into Group 66 and has played a pivotal role in my development as a circuit designer. His constant encouragement and willingness to teach has been critical in making the past three semesters a meaningful learning adventure. I would like to thank my thesis supervisor Professor James Roberge, who has been a source of inspiration since I enrolled in his legacy course on feedback systems. Professor Roberge's approach to designing circuits that win and his dedication to teaching has left a lasting mark on my time at MIT and will follow me through my professional career. I would also like to thank Dr. Kent Lundberg, whose direct involvement in the teaching of 6.301, 6.302, and 6.331 has elevated the courses to a special status at MIT. To have taken these three courses is a rite of passage into the world of analog circuit design at MIT, and the teaching resources that Dr. Lundberg has created over the years are timeless. I would like to thank the Lincoln Laboratory Group 66 Group Leaders, George Nowak, Scott Hamilton, and Fred Walther, whose support for graduate student involvement in Group 66 has afforded me this great opportunity. I would like to thank Dave Crucioli, Dave Spencer, and Frank Mola for all of their help in the prototyping of the circuits I designed. I would also like to thank Bill Wilcox, Alicia Volpicelli, and Gary Hackett for making me feel welcome at Lincoln Laboratory. Lastly, I would like to thank my parents, Glenn and Michele Near, and my wonderful girlfriend, Taylor Krause, whose love and constant support for me as a student, engineer, and hockey player guided my way through nearly six years at MIT.

Contents

List of Figures

List of Tables

Chapter 1

Introduction: Overview of Lasercom

There are several fundamental differences between established radio frequency (RF) communication systems and laser communication (lasercom) systems. The first difference is the wavelength of the information-carrying signal. In a lasercom system, the wavelength of the light is roughly 1,000 times smaller than the wavelength of an established RF signal(1.5μm-800nm compared to 10m-10cm). Accordingly, as in any wireless communication system, the achievable bit rate or channel capacity is directly proportional to the analog bandwidth, which implies that an ideal lasercom link could achieve theoretical bit rates 1,000 times those of established RF links. The second difference relates to beam divergence. There is a fundamental property of electromagnetic waves propagating in free space that the beam diameter increases over distance. Beam divergence is defined for the far field as the angular measure of the increase in beam diameter with distance from the optical aperture from which the beam originates. The beam divergence is proportional to the wavelength of the propagating wave and inversely proportional to the diameter of the beam aperture, and therefore, lasercom systems will have smaller beam divergence than RF systems. One important result of this power efficient delivery is that lasercom systems have the advantage of a lower probability of intercept than established RF systems, where probability of intercept is a measure of one's ability to communicate in the far field exclusively with an

intended target. One scenario where this difference provides a compelling advantage on behalf of lasercom systems is on the battlefield, where communication systems with larger beam divergence allow the enemy to detect the presence of communication, even for encrypted data. With a low probability of intercept, it is possible to design a lasercom link that is extremely difficult to detect. For example, an aircraft performing a covert reconnaissance mission could communicate data with lower probability of detection. An additional advantage of the smaller beam divergence is that transmitters use less power. For a desired power level at the receiver, the transmitters need less power to achieve that level because the energy is contained within a lower divergence beam. Lastly, lasercom systems have the advantage of being physically smaller and lighter. While established RF systems require large antennas, lasercom systems use significantly smaller and lighter optical apertures.

A fair comparison of established RF and lasercom systems requires acknowledgment of lasercom's major drawback, that being the attenuation of infrared radiation in the atmosphere. When infrared radiation is transmitted through the atmosphere, interaction of the transmitted energy with gas particles (primarily vapor and CO_2), attenuates the transmitted energy and thus limits the energy available at the receiver[1]. This atmospheric fading effect scales with the transmitted power. For this reason, it may be difficult for lasercom systems to fully replace lower frequency RF space-to-ground or ground-to-space systems where significant distances must be traversed through the atmosphere. Additionally, the attenuation of infrared radiation presents a significant design challenge of air-to-ground, space-to-ground, and space-to-air lasercom systems that must be robust over a range of weather patterns. Infrared radiation is also subject to atmospheric effects, which result in varying signal intensity within the beam footprint of the receiving aperture plane. One approach to correcting these effects is to use a single large aperture with wavefront correction hardware in the optical train. Another approach, investigated by Group 66, uses several receiving apertures to provide spatial diversity such that, at any one of the apertures, the effects are minimized. Standard channel coding techniques such as forward error correction and interleaving are also implemented to overcome the atmospheric effects

and moving cloud cover, however, even with these physical layer and data link layer improvements, RF systems work more reliably through the atmosphere. For these reasons, the most practical applications of lasercom systems will include:

- Satellite Crosslinks in Space (Low Earth Orbit(LEO-LEO), Geostationary Orbit(GEO-GEO), LEO-GEO)
- Satellite-to-Aircraft Links
- Aircraft-to-Ground Links

With an increasing demand for secure, high data rate communications, lasercom is a viable choice, but will require engineering to overcome the realities of transmitting infrared radiation through the atmosphere.

1.1 Brief Historical Context

The beginnings of lasercom date back to the early 1960s when NASA and the U.S. Air Force pursued a lasercom system capable of a 1 Gbps data rate. This target data rate was needed for future applications and was not reachable with the established RF systems. In the early 1970s, the U.S. Air Force began an initial competition for a laser crosslink demonstration in space. However, budget cuts to the space program reconfigured the demonstration to be an aircraft-to-ground competition. McDonnell Douglas, a major U.S. aerospace manufacturer and defense contractor of the time, delivered the first aircraft and ground terminals in the late 1970s, which proved the feasibility of transferring information at 1 Gbps over a fading atmospheric channel. For its successful demonstration, McDonnell Douglas was awarded a contract in the early 1980s to develop the laser crosslink system (LCS) for space. Meanwhile at the Massachusetts Institute of Technology Lincoln Laboratory (MITLL), the lab's first lasercom system was under construction for NASAs Advanced Communication Technology Satellite (ACTS) program and offered a data rate of 220 Mbps. Unfortunately, several technology limitations of the time contributed to the termination of the LCS

program in 1993, and NASA funding cuts reduced the MITLL program to a laboratory demonstration. Lasercom development was slowed in the mid-1990s until the innovations made in fiber optics communication technology for the telecom industry became readily available, and a growing number of application-specific demands for a high data rate system began to surface[1].

The present demand of the U.S. Military for secure, high data rate communication links has rekindled the research and government investments in developing lasercom systems. One application that requires the performance of a lasercom system is the transmission of sensor data gathered in tactical reconnaissance missions. The current limitations of RF links cannot meet the data rate requirements of these data transmissions. As a result, reconnaissance data recorded on an aircraft performing wide-area surveillance cannot be viewed until the aircraft has landed. This limitation reduces the time value of the reconnaissance data as well as the duration of flight in applications requiring real-time information retrieval. For example, if the reconnaissance data was gathered over a hostile territory, where the suspect was transitioning to a new location, even minutes of delay between the capture and retrieval of the reconnaissance data could greatly diminish its value.

1.1.1 Lasercom at MITLL

Group 66 at MIT Lincoln Laboratory designs lasercom systems under grants from the U.S. Department of Defense. The overall project began in 2009 with the following system goals:

- Real-time data transfer of 2.5 Gbps interim, 10-50 Gbps objective over $\simeq$ 50 km range from aircraft platform to ground terminal
- Low size, weight, and power (SWaP) and integration impact on the aircraft
- Low SWaP ground terminal for ease of deployment
- Reasonable cost

The system uses a 1.5μm wavelength diode-pumped solid-state laser, which places its radiation in the Near Infrared Region (NIR) of the electromagnetic spectrum. In 2009, Group 66 demonstrated a 2.5 Gbps benchmark air-to-ground system over >50km in flight tests with moderate cloud cover. Objective data rates are to be demonstrated in future designs.

1.2 Driving Forces: Size, Weight, and Power (SWaP)

For any aircraft or space-based communication system, there is an important demand to conserve size, weight, and power in the design. The weight and power demands of satellites drastically affect their life-cycle costs including launch costs, on-orbit life, and payload capabilities. Similarly, the size, weight and power constraints imposed by aircraft platforms steer the design of any on board system. The demand for a low SWaP system motivates the thesis work outlined in this proposal. Prior to the beginning of this thesis, Group 66 had designed, built, and tested functional ground-to-ground and air-to-ground lasercom systems. These benchmark designs used many OEM products and their purpose was to prove feasibility of the envisioned lasercom system. Moving forward, major components of the benchmark air-to-ground system must be optimized for low SWaP and system objectives. My previous and future work is focused on the goal of reducing the size, weight, and power of several components in the spatial tracker of the benchmark system, and increasing system performance wherever possible.

Chapter 2

Spatial Tracker Overview

2.1 Architectural Overview

A spatial tracker for lasercom is a control system that helps to establish and maintain a line-of-sight optical communication link. The tracker is composed of several blocks that facilitate link acquisition, link maintenance, and data transfer in an environment with various link impairments. There is at least one spatial tracker at each end of an lasercom link. For example, in an air-to-ground link, there is at least one tracker on the ground terminal and at least one on the aircraft terminal.

The performance of a spatial tracker heavily influences the robustness of a lasercom link. Within the scope of the Open Systems Interconnection (OSI) model shown in Figure 2-1, the challenges of link acquisition and link maintenance are central to the physical layer design, while the challenges of data transfer lie in the data link layer, and are similar to those of any lossy communication link.

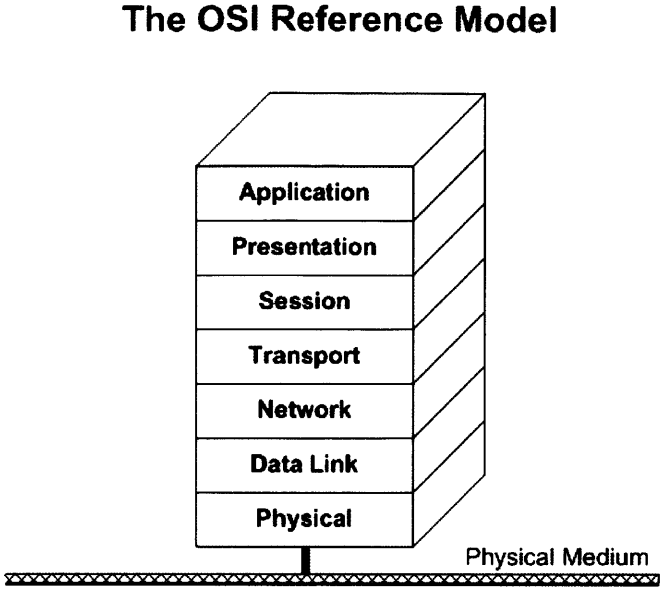

Figure 2-1: Open Systems Interconnection (OSI) Model

2.1.1 Useful Concepts

In order to aid in the explanation of the challenges faced in the design of a spatial tracker for lasercom, the following useful concepts are defined below:

- Field-of-View (FOV): an angular measure of an optical receiver's ability to detect a beam.
- Field-of-Regard (FOR): an angular measure of an optical steering element's ability to steer a beam.
- Beam Width: a measure of length in terms of the angular diameter or divergence of an optical beam.
- Noise Equivalent Angle (NEA): an angular measure of the residual tracking error along the line-of-sight vector that is a function of the received signal to noise ratio in the tracking bandwidth, the optical spot size on the detector, and the gain of the tracking system[1]. The NEA defines the sensitivity of the spatial tracker and a derivation is presented in the appendices.

2.1.2 Link Acquisition

During link acquisition, the primary challenge is to bring the beams of two terminals into each others' FOVs. This process can be a critical bottleneck in establishing communication due to pointing uncertainties, but fortunately there are approaches to reduce the acquisition time and increase the probability of acquisition. The first approach uses telemetry data communicated between the terminals over a lower data rate RF link that provides global position information and ephemeris to reduce the area of uncertainty to a well-defined size. The second approach allows a terminal to spread its transmitted energy over a larger diameter beacon during acquisition. In order for the terminal to spread its transmitted energy, the receiving terminal must have the sensitivity to detect the lower power density. Additionally, even when both of these approaches are employed, there remains the challenge for both terminals of determining their absolute position and orientation. Lasercom terminals frequently employ inertial measurement units (IMUs) to determine absolute position, however, the integrating nature of these devices results in a drift error. It is essential for the error budget of the link acquisition block to address the drift error of the IMUs. Additionally, there is thermal-mechanical drift in the mechanical coupling between the acquisition detector and transmitter that must be considered.

There are symmetric acquisition systems, in which either terminal can initiate the process, and asymmetric acquisition systems, in which only one of the terminals can act as the initiator. The distinguishing feature is that asymmetric acquisition systems generally have one terminal that is SWaP-limited and unable to initiate acquisition. Therefore, the SWaP-limited terminal must wait for the initiator to begin acquisition, after which the following occurs:

- The SWaP-limited terminal detects the initiator's beacon, locks onto the beacon and reduces its pointing error.

- The SWaP-limited terminal responds to the initiator with its own beacon.

- The initiator detects the response, locks onto the returned beacon and reduces its pointing error.
- Assuming that both terminals have locked onto each others' beams and optimized pointing error, the link is established, and communication can begin.

2.1.3 Link Maintenance

During link maintenance, or tracking, the primary challenge is to keep the terminals locked on each others' beams in the presence of disturbances. Spatial trackers on both ends of the link use a set of nested tracking control loops (described below) of increasing bandwidth and rejection (moving inward) to maintain a reliable link. If disturbances force the optical signal to move outside the FOV of one of the nested loops, control is passed to progressively outer loops until a lock is restored. The noise equivalent angle (NEA) of the spatial tracker is an important figure of merit in the performance of both acquisition and tracking loops.

2.1.4 Data Transfer

The primary challenge of data transfer in any communication system is to ensure a low bit error rate. A lasercom system is no different and requires intelligent channel coding protocols such as forward error correction (FEC) and interleaving to achieve a low bit error rate. However, the solutions to this challenge are common to communication through any lossy medium, and therefore lie in the data link layer of the OSI model. As described below, the focus of this thesis is the link maintenance block, more specifically, the design of components in one of the three tracking control loops to meet the requirements of the physical layer of the OSI model.

2.2 Tracking Control Loops

As an aircraft terminal moves relative to a ground terminal in an air-to-ground lasercom link, there are several fundamental disturbances and sources of error that must

be rejected, in order to maintain a reliable communication link. Drift and mechanical jitter both originate on the terminal itself, while pointing error is the result of uncertainty between two terminals. The frequency spectra of these errors are summarized in Table 2.1.

Table 2.1: Types of Error in a Lasercom System

Error Type	**Frequency Range**
Drift	DC-10Hz
Pointing	DC-50Hz
Mechanical Jitter	50Hz-1kHz

From a systems-level point of view, the spatial tracker must provide a rejection function that results in error that is less than fractions of the beam width of the optical signal. The tracker achieves the required rejection using a set of three nested tracking control loops referred to as the pointing (outer), coarse track (middle), and fine track (inner) control loops. During link acquisition and maintenance, tracking control is handed off between the nested control loops in order to maintain lock.

2.2.1 Pointing Control Loop

The pointing system is centered around an optical steering element or gimbal. The primary function of the pointing control loop is to keep the control loops with narrower FOVs centered with a low bandwidth of 10's of Hz [9]. The input to the pointing control loop is a pointing command calculated from telemetry and ephemeris data.

2.2.2 Coarse Track Control Loop

The coarse track system used in the MITLL benchmark system is shown in Figure 2-2 [9]. It relies on the pointing system to track the optical signal in a low-frequency sense, and it adds the ability to track with a higher bandwidth to maintain a locked

link in the presence of high frequency platform jitter due to base motion disturbances. The different functions of the terminal components are summarized in Table 2.2.

Table 2.2: Terminal Components in the Coarse Track System

Component	**Purpose**
Steering Flat(OFLAT)	Used in the coalignment of multiple apertures
Fast Steering Mirror(FSM)	Primary beam steering element
Hollow Retro-Reflector(HRR)	Used to bore sight the FPA and fiber
Beam Splitter(B/S)	Splits beam for tracking and communication
Focal Plane Array(FPA)	Primary tracking sensor
Collimator	Narrows incoming beam onto fiber for comm

2.2.3 Fine Track Control Loop

The primary function of the fine track control loop is to provide better rejection of the low-frequency error components. It is controlled using a nutation approach and automatic gain control (AGC) to track.

2.3 Scope of Thesis

The focus of this thesis is the design of circuits for a spatial tracker and improvements in size, weight, and power that can be made to the coarse track control loop in a benchmark lasercom system. It includes the design and testing of an efficient PWM switching amplifier topology for controlling an FSM in closed loop and an investigation of a lower cost, lower power, and higher bandwidth tracking sensor.

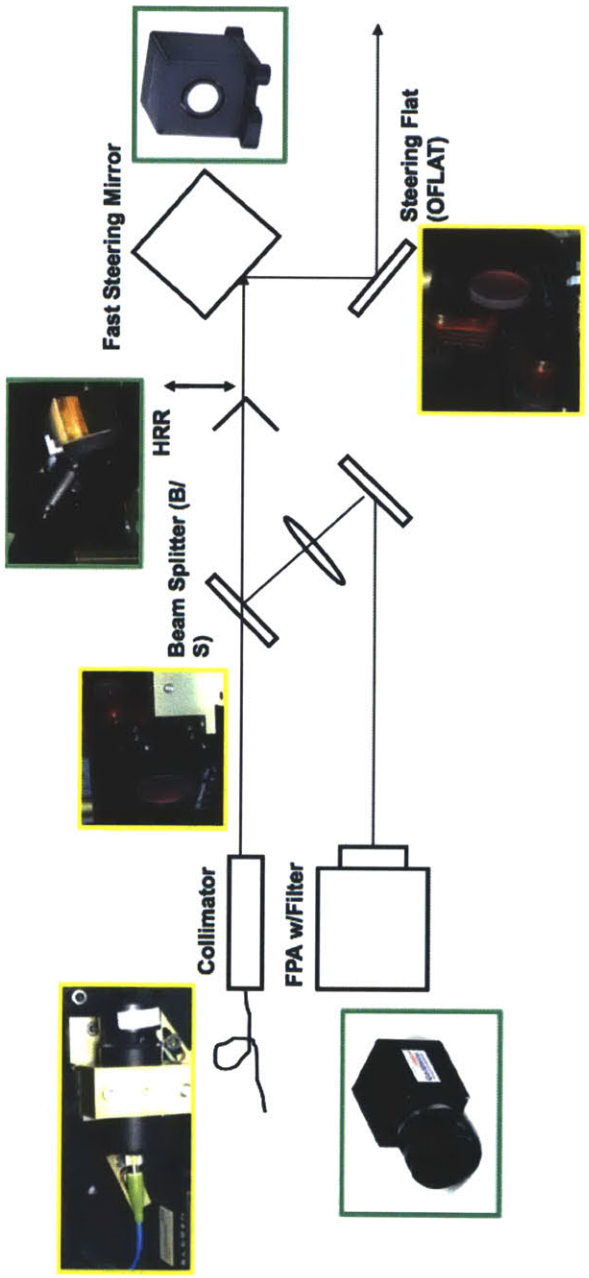

Figure 2-2: Coarse Track Control Loop Construction

Chapter 3

Fast Steering Mirror Overview

A fast steering mirror (FSM) is a one or two-axis, high-bandwidth mirror used to steer an optical beam with microradian resolution. The MITLL Group 66 benchmark system uses a two-axis FSM as the high bandwidth steering element in the coarse track control loop of the spatial trackers. The mirror coordinate axes for a two-axis FSM are shown in Figure 3-1, as viewed from the front of the mirror. In lasercom systems, the Y-axis and X-axis are commonly referred to as the Azimuth and Elevation axes respectively. It is common for FSMs to have their steering interface rotated 45^o off the AZ-EL axes on the A-B axes to minimize volume. When using these mirrors, a coordinate transformation block is needed to close a feedback loop around position feedback located on the AZ-EL axes.

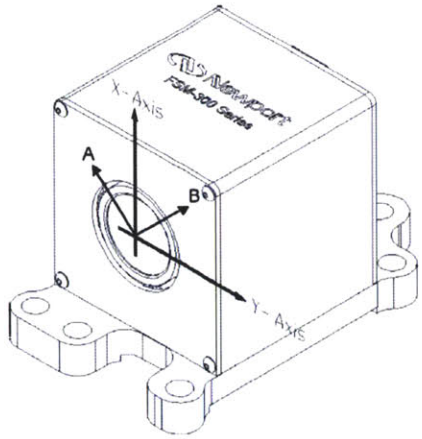

Figure 3-1: Fast Steering Mirror (FSM) Axes

3.1 Mechanical Model: Spring-Mass-Damper

A spring-mass-damper approximation can be used to model the dominant FSM dynamics. The dominant low frequency behavior is modeled by a system with one spring, mass, and damper, which has a primary mechanical resonance resulting from the under damped energy transfer between the spring and the inertia of the mass. Additionally, there are one or more resonances due to mechanical decoupling that occurs when parts of the mirror depart from a rigid body approximation. A rough model that includes both low and high frequency behaviors consists of two masses, two springs, and two dampers, where the first mass, M_1, is much larger than the second mass, M_2 (shown in Figure 3-2). The mass M_2 represents the part of the mirror that decouples from the main mass, M_1.

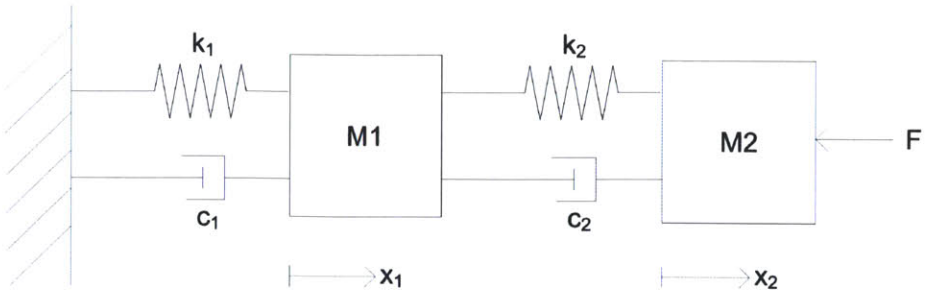

Figure 3-2: Two-Mass, Spring-Mass-Damper System

For this system, the primary and secondary resonances occur at frequencies given by the following equations (see the appendices for a derivation of the spring-mass-damper equations):

$$\omega_{primary} = \sqrt{\frac{k_1}{M_1 + M_2}} \tag{3.1}$$

$$\omega_{secondary} = \sqrt{\frac{k_2}{M_2}} \tag{3.2}$$

where k_1, the spring constant of the mounting flexure between the mirror mount and the housing, and k_2, are used to provide an approximate model of the elastic modes of the FSM.

3.2 Electrical Model: Voice Coil Actuators

The electrical interface to an FSM is commonly two pairs of voice coil actuators which are driven differentially to steer the mirror in two axes. This type of voice coil actuator uses the magnetic field generated in a spatially-fixed coil of wire to generate a motive force on a permanent magnet mounted on the mirror. The actuator can be modeled by an inductor with a series resistance and a back electromotive force (EMF) as shown in Figure 3-3 [4].

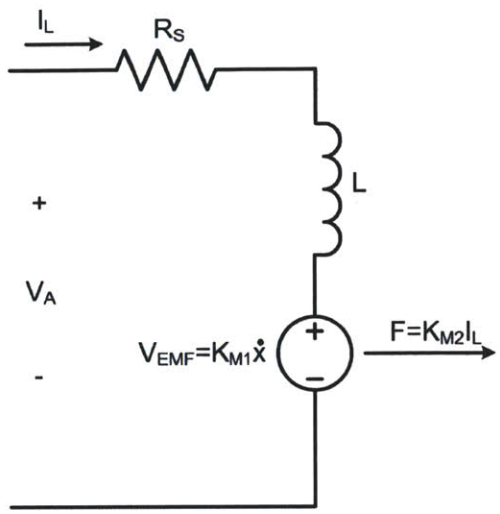

Figure 3-3: Model of Single Voice Coil Acutator

Driving an inductive load with series resistance is dominated by a purely electrical time constant given by $\tau_e = \frac{L}{R_s}$. However, driving a load that includes the back EMF is dominated by an electromechanical time constant τ_m that depends on mechanical properties of the actuator. Due to the difficulty in modeling or calculating this time constant without conversation with the designer or reverse engineering, it is most easily determined through measurement.

When driving this load with a power amplifier that acts like a voltage source (V_A), the current through the load is given by:

$$I_L = \frac{V_A - V_{EMF}}{sL + R_s} \tag{3.3}$$

Therefore, the system is first-order with a single pole located at:

$$\omega_{pole} = \frac{R_s}{L} \tag{3.4}$$

As will be explained in subsequent chapters, a more complicated power amplifier and load relationship exists that results from the EMF.

3.3 Measuring Dynamics

All of the FSMs that are considered in the following sections have similar second-order dynamics, with primary and secondary resonances as described above. The dynamics measurements were performed using an HP Model 3562A Dynamic Signal Analyzer. The analyzer has three ports for interfacing to a system: a source, measurement channel 1, and measurement channel 2. The source is used to stimulate the system and the measurement channels are placed across system blocks to measure transfer characteristics (i.e. magnitude, phase, spectral power density). The analyzer is used in this manner to obtain Bode plots of the FSM dynamics.

3.4 Mirror Comparison

Group 66 has been experimenting with three different FSMs, one of which was designed and built at MITLL. The three mirrors are shown in Figure 3-4 and compared in the following subsections.

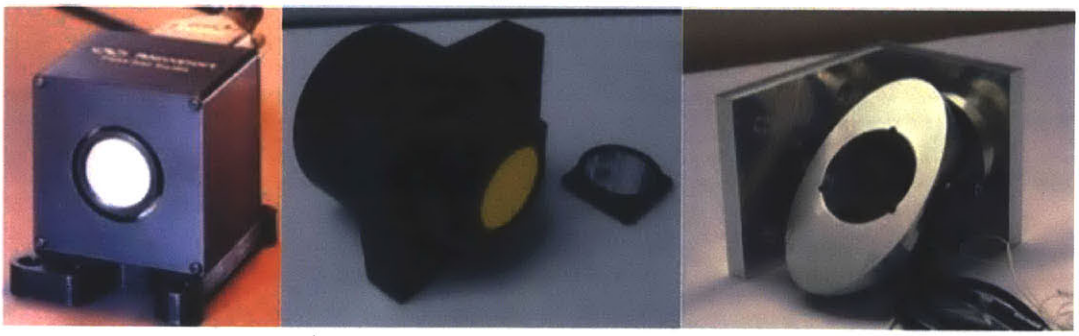

Figure 3-4: Newport FSM300, Optics In Motion OIM101, MITLL Dither Mirrors (Left to Right)

3.4.1 Mirror Dynamics

The frequency responses of the three mirrors were measured using position sensor feedback. Figures 3-5, 3-6, 3-7, 3-8, 3-9, and 3-10 show the open loop Bode plots

of the Newport FSM300, Optics in Motion OIM101, and MITLL Dither mirrors respectively.

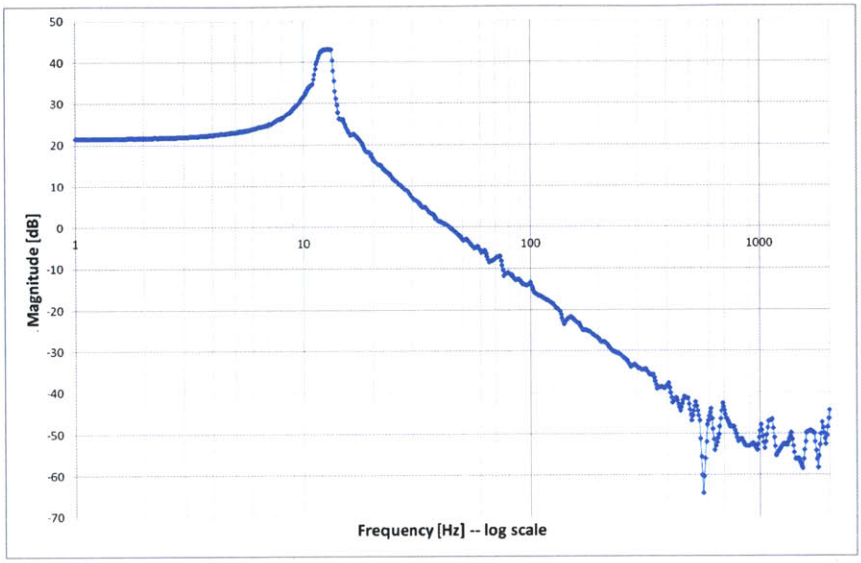

Figure 3-5: FSM300 Open Loop Bode Magnitude

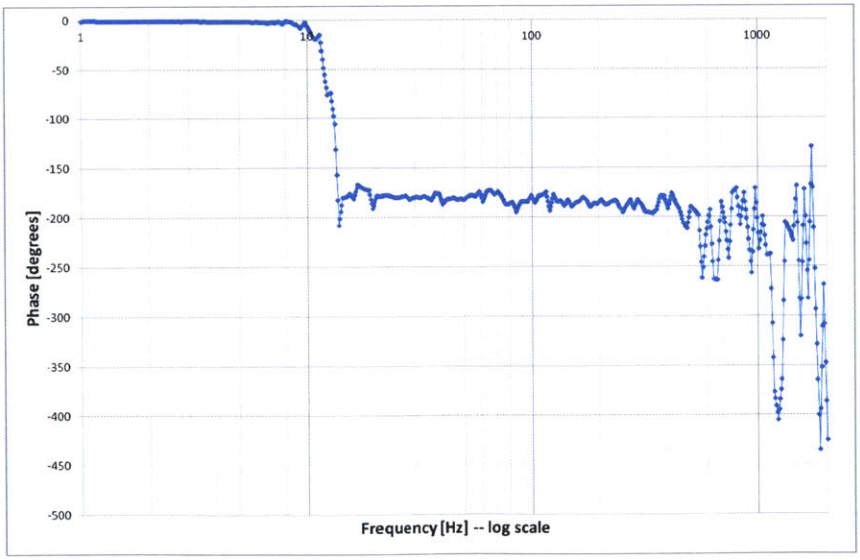

Figure 3-6: FSM300 Open Loop Bode Phase

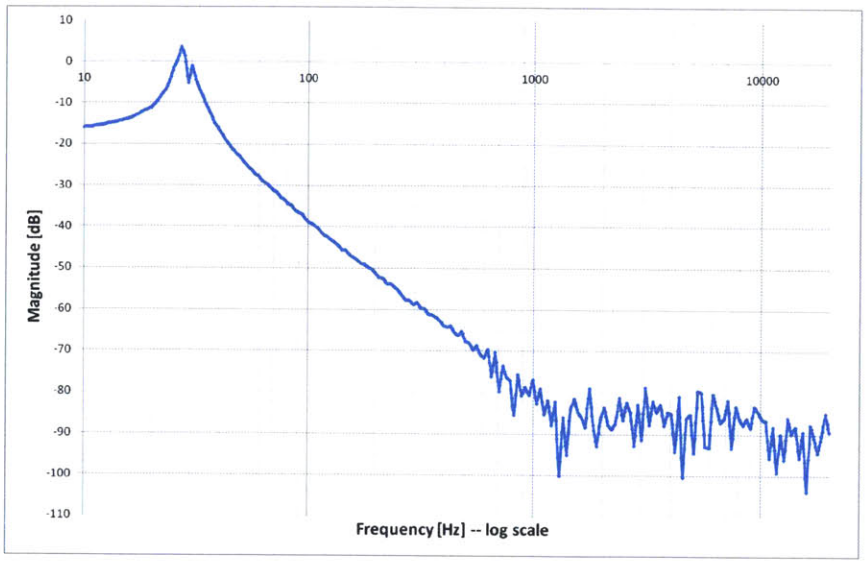

Figure 3-7: OIM101 Open Loop Bode Magnitude

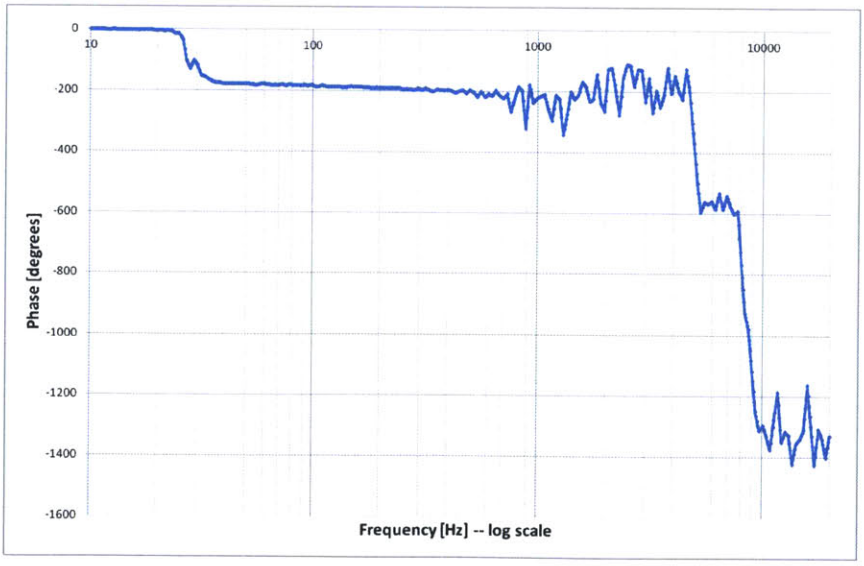

Figure 3-8: OIM101 Open Loop Bode Phase

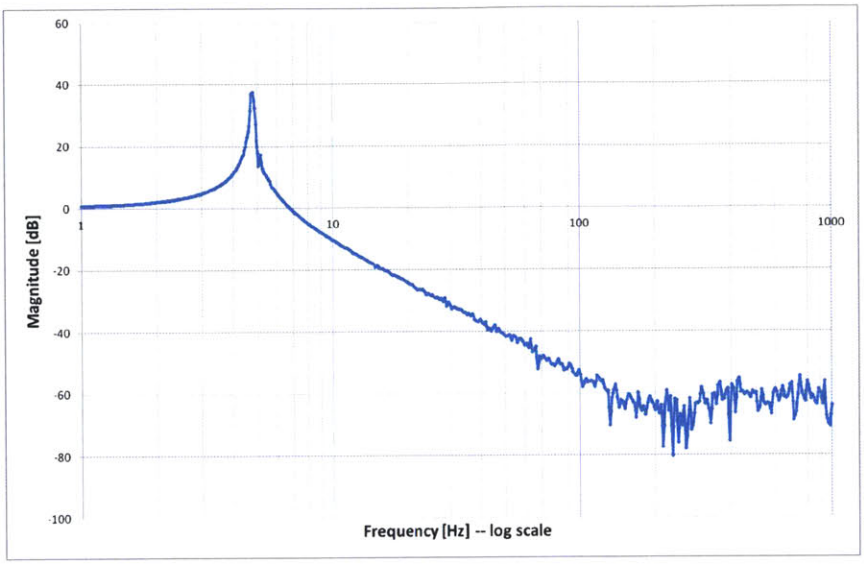

Figure 3-9: MITLL Dither Open Loop Bode Magnitude

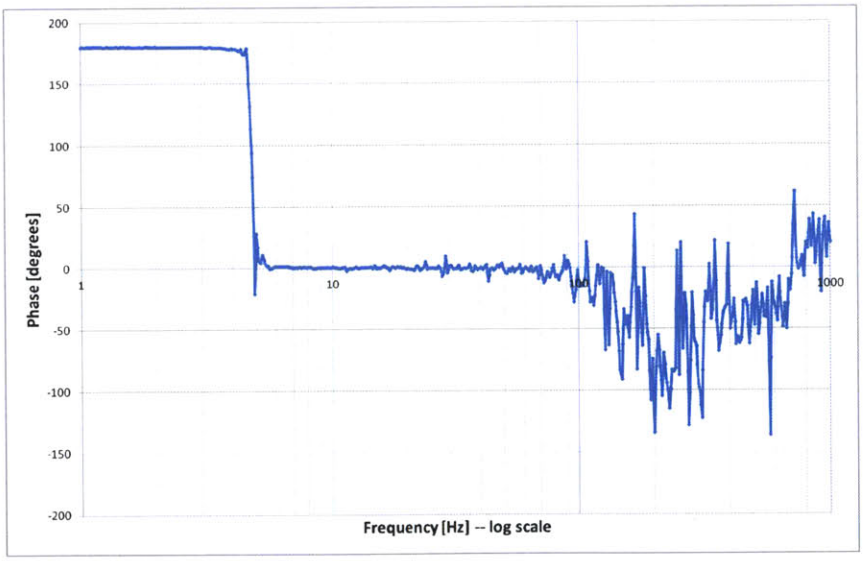

Figure 3-10: MITLL Dither Open Loop Bode Phase

3.4.2 Summary of Mirror Differences

Table 3.1 summarizes the key features of the three mirrors.

Table 3.1: Mirror Comparison: Key Features

	FSM300	**OIM101**	**MITLL Dither**
Number of Axes	2	2	1
Angular Range (Mech.)	$\pm$26.3 mrad	$\pm$26.3 mrad	$\pm$104 mrad
Resolution	$\leq$1 μrad rms	$\leq$2 μrad rms	$\leq$2 μrad rms
Cont. Max Power to Mirror	15W	30W	45W
Mirror Head Weight	15.3oz (434g)	12.2oz (346g)	5.92oz (168g)
Primary Mech. Resonance	12.5Hz	28Hz	4.7Hz
Secondary Mech. Resonance	>1kHz	> 1kHz	506Hz
Voice Coil Inductance	100μH	500μH	190μH
Voice Coil Resistance	5.1Ω	5.8Ω	1.7Ω
$\frac{R}{2\pi L}$ Frequency	8.1kHz	1.9kHz	1.4kHz

Chapter 4

FSM PWM Driver and Compensator

The need for a smaller, lighter, and more efficient driver that is compatible with several mirrors was the motivation for replacing the controllers that are shipped with FSMs and designed for laboratory use.

4.1 PWM Driver Circuit

There are two main approaches for driving a FSM as modeled in the previous chapter. The first approach uses a linear amplifier, however, linear amplifiers lose a significant amount of power due to biasing and the linear operation of the output transistors. The second approach uses a switching amplifier that can achieve a significantly higher efficiency. The circuit shown in Figure 4-1 is an efficient, PWM driver for steering a FSM. This topology will work for any FSM with voice coil actuators as the drive interface and similar power requirements to the three mirrors previously discussed. It uses current feedback in the driver loop to simplify the mirror drive, where the force generated by the actuator is proportional to the load current. The switching frequency, full bridge supply voltage, and integrator gain can be adjusted for a wide range of coil inductances. The following subsections explain the major components of the PWM driver.

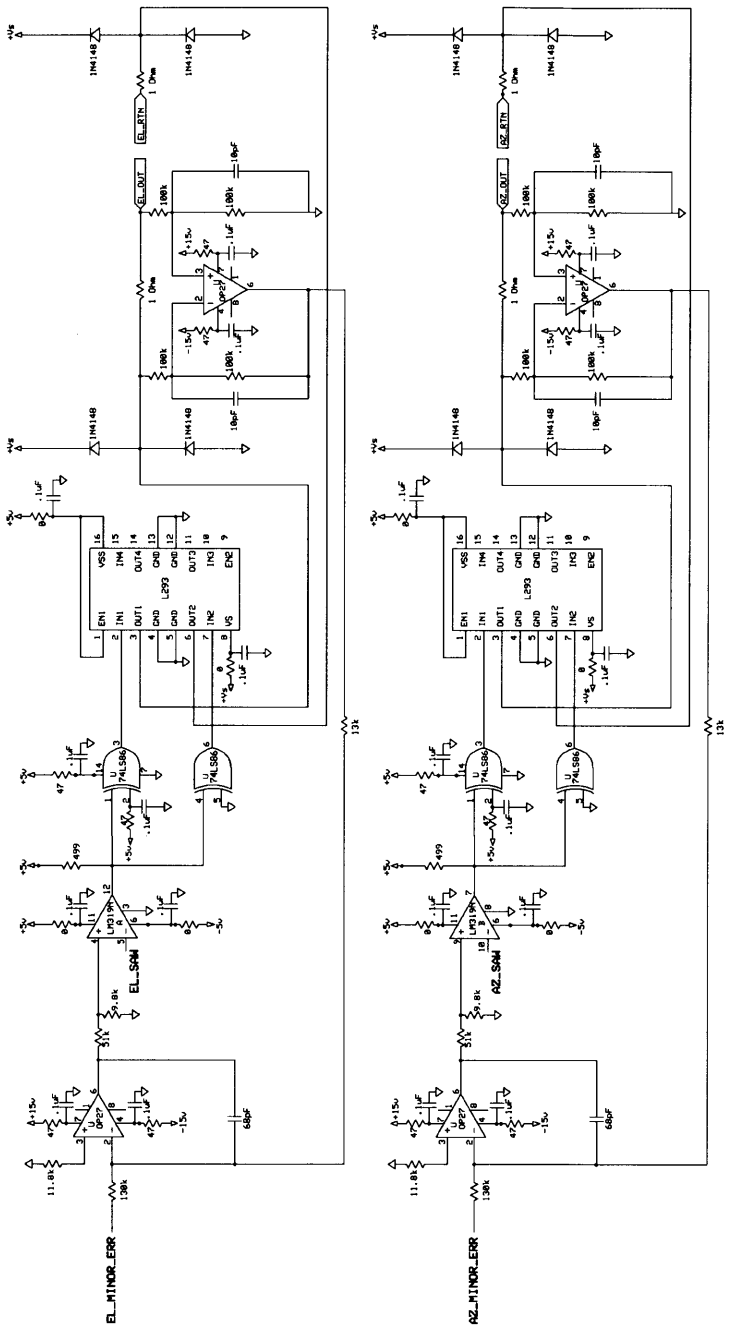

Figure 4-1: PWM Drivers

4.1.1 Full Bridge Output Stage

The output stage of the PWM driver uses a full bridge (or H bridge) topology. This approach places the FSM voice coils as a bridge-tied load between the outputs of two half bridges and allows bidirectional current to flow. It is a particularly favorable approach in ground-referenced output stages, where it eliminates the need for a negative supply. In high power applications, the full bridge is usually designed from discrete transistors and an IC gate driver, however, the power needed to drive a FSM makes the L293 Quad Push-Pull IC a favorable option. The L293 features 1A output current per channel and separate power supplies for the logic and output stage.

This PWM approach switches both sides of the load between the supply and ground at the PWM switching frequency. Due to the inductive nature of the voice coils, the current in the coils cannot go to zero instantaneously. Therefore, freewheeling diodes are added to allow the inductor current to ramp down at the end of each switching cycle.

4.1.2 Current Feedback

To command current in the voice coils in closed-loop, the coil current must be sensed and used as feedback in the driver. This is accomplished using a sense resistor (usually 1Ω or less to limit power dissipation and voltage drop) and an instrumentation amplifier. The combination of the two is referred to as a current monitor. For a 1Ω sense resistor and equal value resistors around the amplifier, the current monitor provides a 1Ω transimpedance (current-to-voltage) transformation. The output voltage is fed back to a summing amplifier through a resistor. The PWM driver uses the summing amplifier for two purposes, generating the error signal and the loop integrator to remove steady-state error. The integrator gain is set to achieve desired loop dynamics in the closed-loop driver. The major limitation on increasing the integrator gain is the dominant time constant due to the voice coils, which contributes a -90 degree phase shift.

4.1.3 Sine Triangle PWM

A common approach to generating the variable duty cycle waveform for a PWM circuit is to use a comparator with its non-inverting input set by a reference voltage and its inverting input driven by a sawtooth waveform. At the output of the comparator, a square wave will be generated with a frequency set by the frequency of the sawtooth input. When the reference voltage is at the midpoint of the sawtooth waveform (i.e. 0V on a 2.5Vpp waveform), the resulting square waveform will have a duty cycle of D=0.5. By varying the reference voltage, a variable duty cycle waveform can be be generated at the output of the comparator, which can be used to control the H Bridge output voltage across the bridge-tied load. The output is centered around D=0.5, which drives 0V across the load. Observing the output of the current monitor, a positive current flows for D>0.5 and a negative current flows for D<0.5.

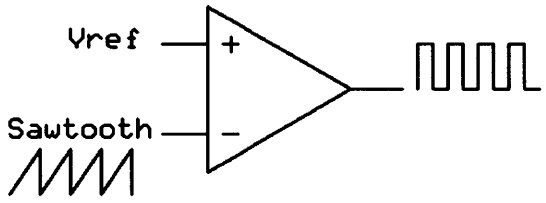

Figure 4-2: Comparator Configured for Sine Triangle PWM (D=0.5)

The choice of switching frequency (f_{sw}) for the sawtooth waveform has two major influences. The first is the $\frac{L}{R}$ time constant of the voice coils. The second is the subsequent desired closed-loop bandwidth of the FSM control loop. From a control standpoint, a switching amplifier adds delay to the loop that is modeled by $e^{\frac{-s}{2f_{sw}}}$ [11]. According to Laplace, the delay in the s-domain corresponds to a time shift in the time domain, as shown below.

$$\mathcal{L}\{f(t-a)\} = F(s)e^{-sa} \tag{4.1}$$

For f(t)=sin(ωt):

$$\mathcal{L}^{-1}\{F(s)e^{\frac{-s}{2f_{sw}}}\} = \sin(\omega t - \frac{\omega}{2f_{sw}}) = \sin(\omega t - \phi) \tag{4.2}$$

The phase shift (ϕ_{deg}) in degrees at frequency f is given by:

$$\phi_{deg} = \frac{2\pi f}{2f_{sw}}\frac{180}{\pi} = \frac{180f}{f_{sw}} \tag{4.3}$$

A good rule of thumb is to sample 6-10x over the rise time t_r in order to limit the phase shift to a few degrees. Therefore, a switching frequency that is at least 30x faster than the natural frequency of the system will allow continuous time control techniques to be applied to the sampled system[11]. The sawtooth waveform is easily generated using a 555 timer as shown in Figure 4-3. The LMC555, a CMOS version of the popular 555 timer, is cable of generating astable multivibrator outputs of up to 3MHz, which is sufficiently faster than needed.

4.1.4 XOR for Symmetric Timing

A duty cycle of D=0.5 corresponds to zero current command in the voice coils, which is the result of equal voltages at the output of both half bridges in the H Bridge output. This places equal voltages on either side of the bridge-tied voice voice coil. In order to drive bidirectional current through the voice coils, both positive and negative voltages must be driven across it. This is accomplished using the variable duty cycle waveform, D, and its duty cycle inverse, 1-D, which are applied to the control inputs of the two half bridges. The 1-D waveform can be generated using a two-input XOR gate, with one of its inputs held high. The D waveform is also passed through a two-input XOR gate, with its second input held low to buffer the signal, in order to keep the propagation delays equal between the D and 1-D waveforms driving the two half bridges.

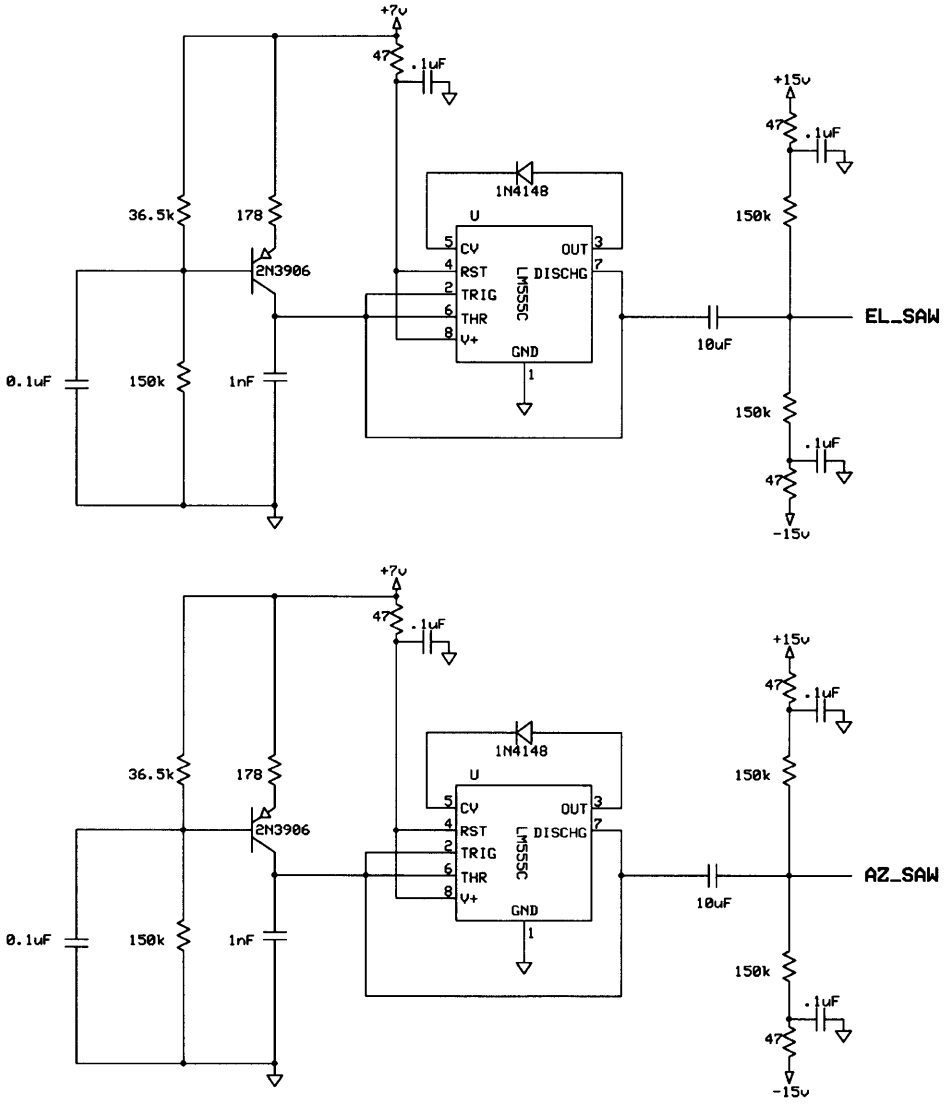

Figure 4-3: LMC55 Sawtooth Generators

Table 4.1: Block Diagram Units

Variable	Units
V_{CMD}	[V]
V_{FB}	[V]
V_E	[V]
V_I	[V]
V_A	[V]
V_{EMF}	[V]
V_C	[V]
IL	[A]
K_{M2}	$[\frac{N}{A}]$
K_{M1}	$[\frac{N}{A}]$
M	[kg]
$\dot{x}$	$[\frac{m}{s}]$
x	[m]

4.2 PWM Driver and FSM as Plant

The previous chapter outlined an electromechanical model for the voice coil actuators of an FSM. The following analysis develops a more detailed control model for the PWM driver and actuators in order to establish the 'plant' of a mirror control system. Figure 4-4 is a block diagram for the closed-loop driver and voice coil actuator. Table 4.1 shows the units of the variables.

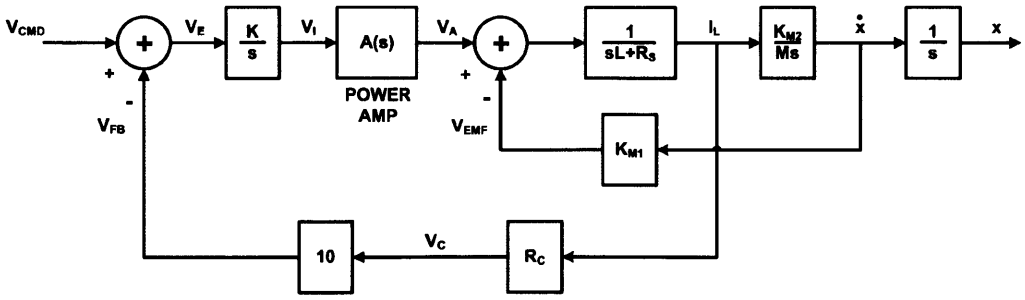

Figure 4-4: PWM Driver and Load Model

The power amp block A(s) represents part of the driver from the input to the comparator to the output voltage across the bridge-tied load. Using the delay model

for the PWM circuit and further inspection of the gain through this part of the driver, it can be shown that:

$$A(s) = 2e^{\frac{-s}{2f_{sw}}} \tag{4.4}$$

The back EMF voltage (V_{EMF}) generated in the voice coil actuator is given by:

$$V_{EMF} = K_{M1}\dot{x} \tag{4.5}$$

And the force generated by the voice coil actuator is given by:

$$F = K_{M2}I_L = M\ddot{x} \tag{4.6}$$

The voltage-to-current transfer function from the output of the power amp is effectively a minor loop in the overall driver and can be written using Black's formula:

$$\frac{I_L}{V_A} = \frac{\frac{1}{sL+R_s}}{1+\frac{1}{sL+R_s}\frac{K_{M1}K_{M2}}{Ms}} = \frac{\frac{s}{L}}{s^2+s\frac{R_s}{L}+\frac{K_{M1}K_{M2}}{LM}} \tag{4.7}$$

The transfer characteristic from the input to the driver to the output of the current monitor is the major loop and can also be written using Black's formula:

$$\frac{V_C}{V_{CMD}} = \frac{\frac{sKA(s)R_c}{sL(s^2+s\frac{R_s}{L}+\frac{K_{M1}K_{M2}}{LM})}}{1+\frac{sKA(s)R_c}{sL(s^2+s\frac{R_s}{L}+\frac{K_{M1}K_{M2}}{LM})}10} = \frac{\frac{KA(s)R_c}{L}}{s^2+s\frac{R_s}{L}+\frac{K_{M1}K_{M2}}{LM}+\frac{10KA(s)R_c}{L}} \tag{4.8}$$

where R_c is the 1Ω sense resistor in the current monitor. This transfer characteristic describes a second-order system with natural frequency given by:

$$\omega_o = \sqrt{\frac{K_{M1}K_{M2}}{LM}+\frac{10KA(s)R_c}{L}} \tag{4.9}$$

and a damping ratio given by:

$$\zeta = \frac{R_s}{2L}\frac{1}{\omega_o} \tag{4.10}$$

4.3 Block Diagram Explanations

From a block diagram perspective, the control loops for the FSMs are similar, and vary only in the location of a coordinate transformation block. Figure 4-5 shows the configuration for mirrors with the drive and position sensors located on the A-B axes. Figure 4-6 shows the configuration for mirrors with the drive on the AZ-EL axes and the position sensors on the A-B axes.

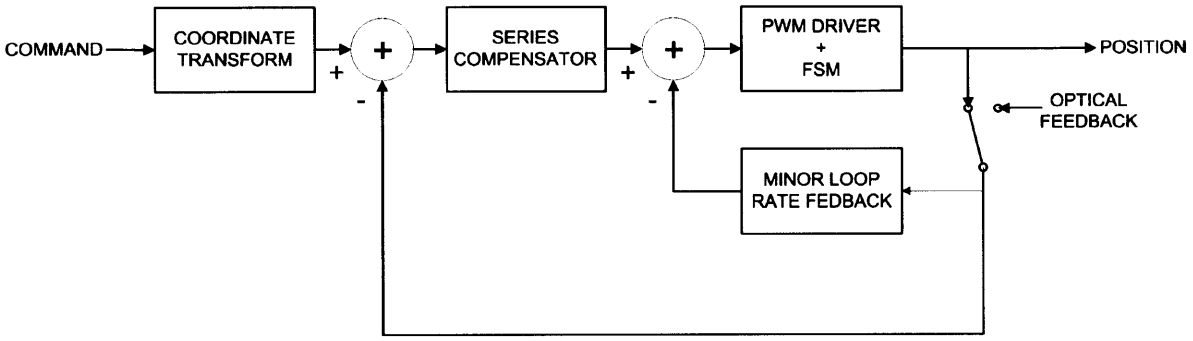

Figure 4-5: Block Diagram for FSM300, OIM101, and MITLL Dither Mirror Control Loops

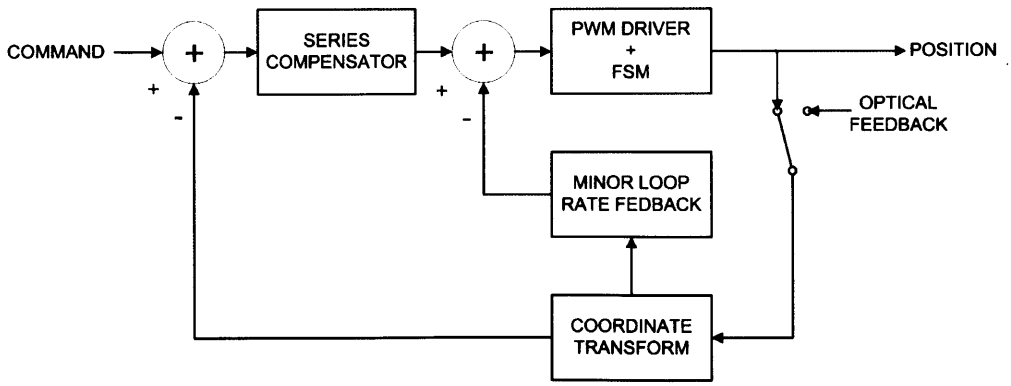

Figure 4-6: Block Diagram for Other Possible Mirror Control Loop

4.4 Compensator

The spring-mass-damper model of the FSM from the previous chapter suggests that the dominant low frequency behavior of the FSM can be modeled by a second-order transfer function, given by:

$$G_{FSM}(s) = \frac{G_{DC}\omega_o^2}{s^2 + 2\zeta\omega_o s + \omega_o^2} \tag{4.11}$$

where ω_o is the natural frequency where the primary mechanical resonance occurs and ζ is the damping ratio. The relevant second-order system performance metrics are[4]:

$$DampedNaturalFrequency : \omega_d = \omega_o\sqrt{1-\zeta^2} \tag{4.12}$$

$$Time - to - Peak : t_p = \frac{\pi}{\omega_d} = \frac{\pi}{\omega_o\sqrt{1-\zeta^2}} \tag{4.13}$$

$$PeakOvershoot : P_o = 1 + exp(-\frac{t_p}{\tau_{env}}) = 1 + exp(\frac{-\pi\zeta}{\omega_o\sqrt{1-\zeta^2}}) \tag{4.14}$$

$$MagnitudePeaking : M_p = \frac{1}{2\zeta\sqrt{1-\zeta^2}}\zeta < \frac{1}{\sqrt{2}} \tag{4.15}$$

A second-order system of this kind requires compensation to close a stable control loop. The approach consists of two compensation techniques and has been successfully used by Professor James Roberge to compensate FSMs. The first technique uses minor loop feedback to improve the damping of the plant (driver and FSM). The second uses a series compensator to achieve first-order loop behavior before crossover frequency.

4.4.1 Minor Loop Compensation

Applying rate position feedback around the driver and FSM (the 'plant') provides a degree of control on the damping of the under damped second-order system. The ideal amount of damping will drive the complex conjugate poles to the negative real

axis of the pole-zero plot. Upon successfully damping the under damped system, a series compensator can be used to close a stable feedback loop around the critically damped system with two negative real poles in the left-half plane. The circuit used for applying rate feedback is an op amp differentiator, as shown in Figure 4-7.

When the differentiator is placed in the feedback path of a second-order system, Black's formula can be applied to calculate the effective damping of the system:

$$G_{FSM}(s) = \frac{G_{DC}\omega_o^2}{s^2 + 2\zeta\omega_o s + \omega_o^2} \tag{4.16}$$

$$H_{DIFF}(s) = -bs \tag{4.17}$$

$$\frac{C}{R}(s) = \frac{G_{FSM}}{1 + G_{FSM}H_{DIFF}} = \frac{\frac{G_{DC}\omega_o^2}{s^2+2\zeta\omega_o s+\omega_o^2}}{1 + \frac{G_{DC}\omega_o^2}{s^2+2\zeta\omega_o s+\omega_o^2}(bs)} \tag{4.18}$$

$$\frac{C}{R}(s) = \frac{G_{DC}\omega_o^2}{s^2 + (2\zeta\omega_o + bG_{DC}\omega_o^2)s + \omega_o^2} = \frac{G_{DC}\omega_o^2}{s^2 + 2\zeta_{eff}\omega_o s + \omega_o^2} \tag{4.19}$$

The FSM with minor loop rate feedback has the same natural frequency as the FSM in open loop, however, the damping has been increased. The effective damping is given by:

$$\zeta_{eff} = \zeta + \frac{bG_{DC}\omega_o}{2} \tag{4.20}$$

The differentiator is designed to provide an effective damping of ζ_{eff}=1 (critical damping), in which case both of the complex conjugate poles are located on the negative real axis. This system is more easily compensated with series compensation techniques.

4.4.2 Series Compensation

The critically damped (ζ_{eff}=1) system with minor loop feedback has two negative real poles and zero magnitude peaking, however, the system's phase rolls hard after

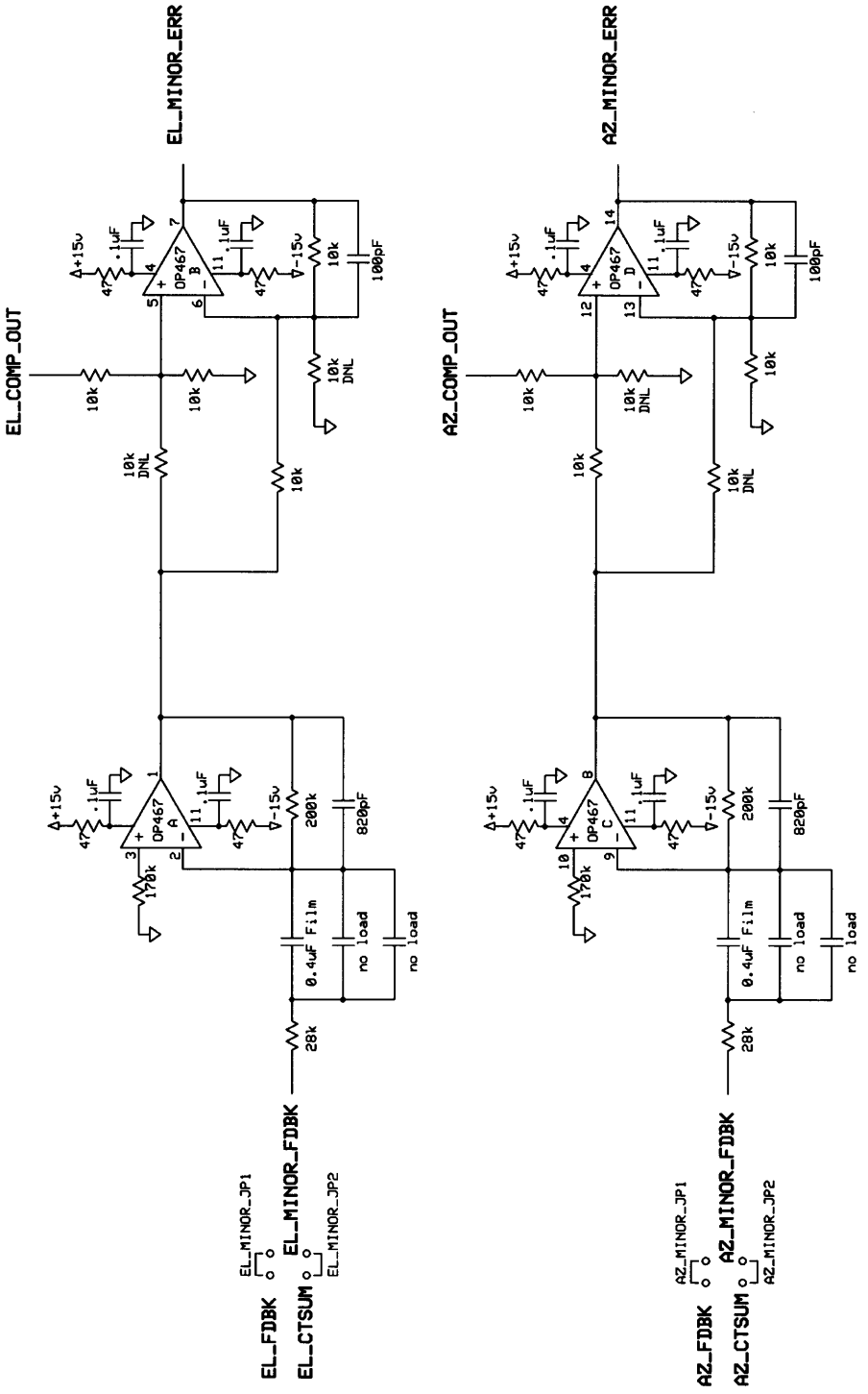

Figure 4-7: Op Amp Differentiators and Minor Loop Summing Junctions

the primary resonance. The series compensator shown in Figure 4-8 is composed of two major parts–a lag network and a lead network. The lag network places a DC pole and a zero at the primary resonance. The lead network place a zero at the primary resonance and a pair of poles beyond the desired crossover frequency. The combination of these two blocks effectively cancels the double pole at the primary resonance and allows the feedback loop to be closed around an open loop transfer function of $\frac{K}{s}$. Applying Black's formula, the resulting control looks first order before crossover:

$$\frac{C}{R}(s) = \frac{G}{1+GH} + \frac{\frac{K}{s}}{1+\frac{K}{s}} = \frac{K}{s+K} \tag{4.21}$$

This in effect cancels the primary response of the plant, and limited by the elastic modes of the plant, replaces it with the desired response of the system.

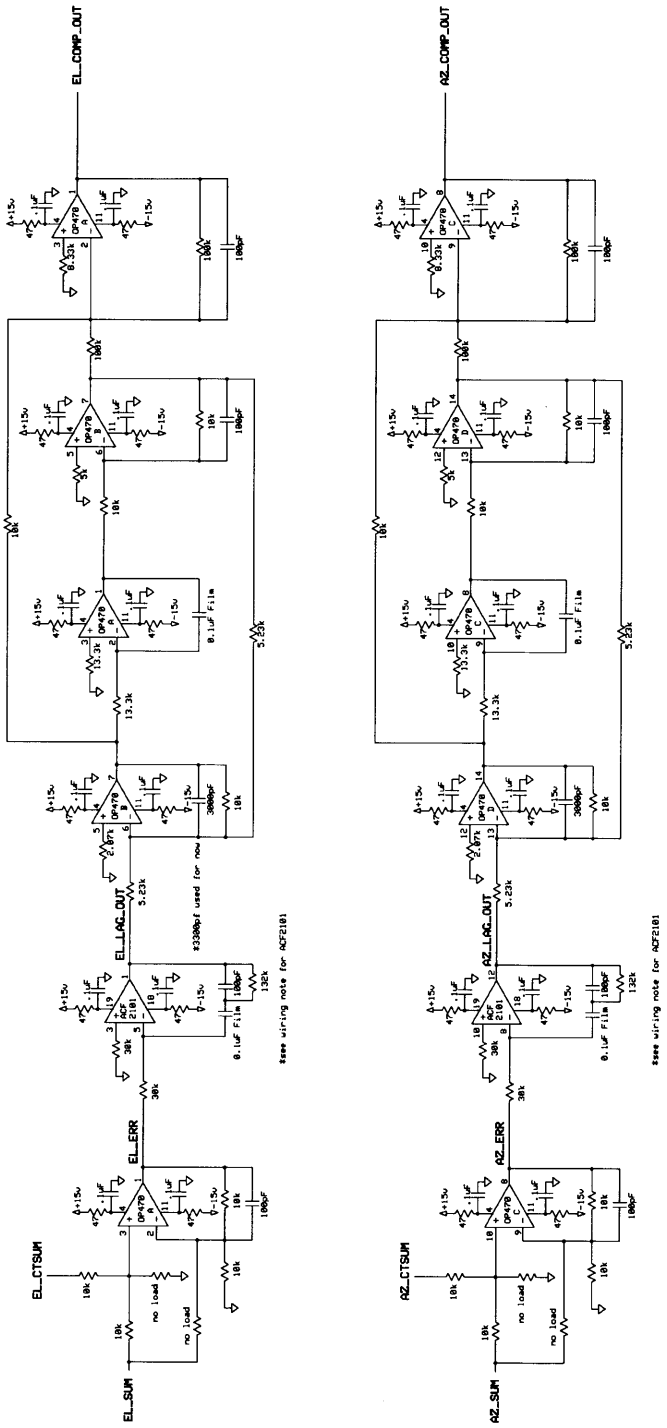

Figure 4-8: Series Compensator

4.4.3 Coordinate Transformer

Two of the FSMs compared in the previous chapter (FSM300 and OIM101) and the preceding block diagrams suggest the need for a coordinate transformation to close a feedback loop around position feedback located off the AZ-EL axes. Figure 4-9 shows the AZ-EL and A-B axes.

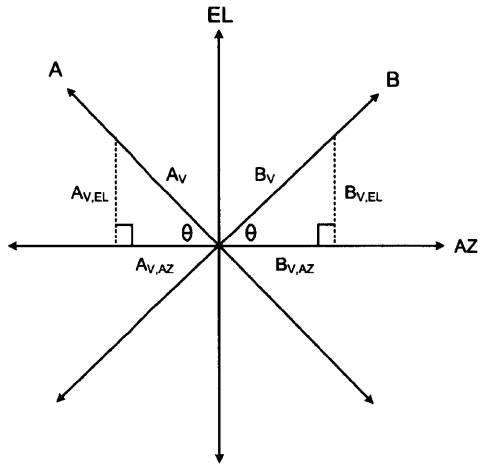

Figure 4-9: Generic Coordinate Transform

To rotate vectors A_V and B_V in the A-B axes to the AZ-EL axes, where the angle between the axes is θ=45^o, the components of the vectors in the AZ-EL axes are given by a scaled difference and sum:

$$AZ_V = B_{V,AZ} - A_{V,AZ} = B_V cos(\theta) - A_V cos(\theta) = \frac{1}{\sqrt{2}}(B_V - A_V) \tag{4.22}$$

$$EL_V = B_{V,EL} + A_{V,EL} = B_V sin(\theta) + A_V sin(\theta) = \frac{1}{\sqrt{2}}(B_V + A_V) \tag{4.23}$$

Figure 4-10 shows a generic coordinate transform circuit that can be loaded to achieve different rotations.

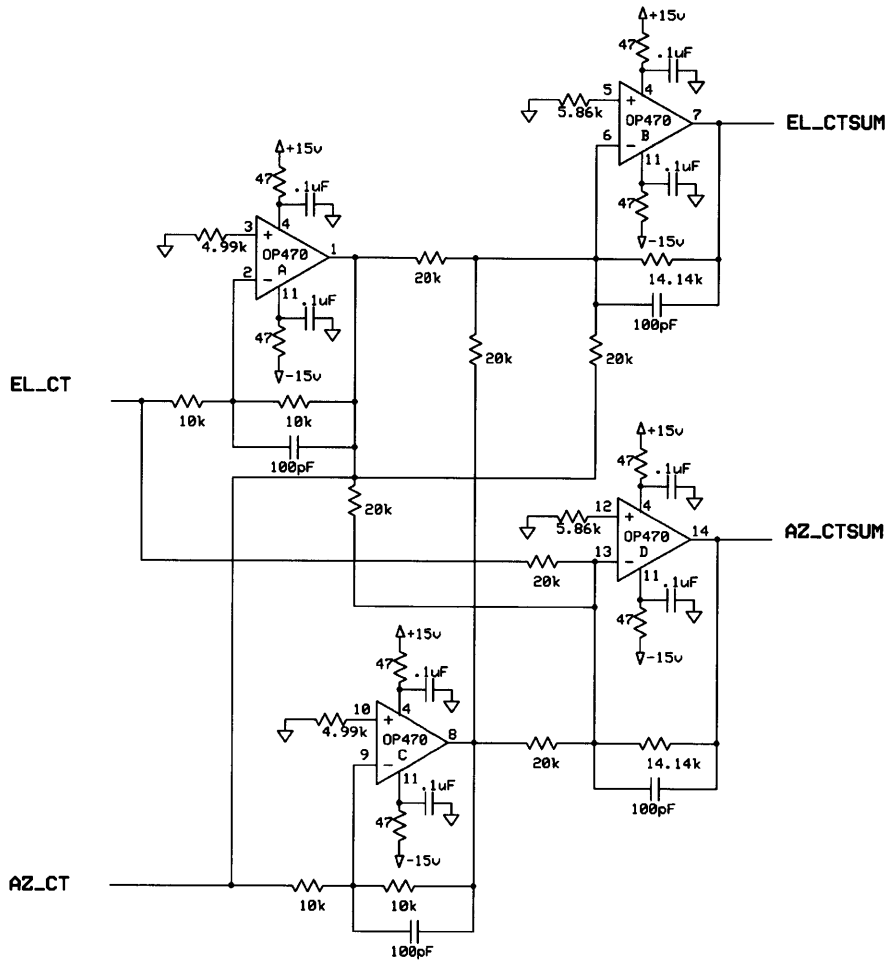

Figure 4-10: Generic Coordinate Transform Circuit

4.5 Results

After preliminary testing of the PWM driver and compensation circuits, the designs were brought together onto two printed circuit boards (PCBs). These boards were designed to accommodate general FSM characteristics and can be populated to meet the driving requirements of many FSMs.

4.5.1 Compensated Dynamics

The following figures show the compensated forward path Bode plots for the compensated mirrors.

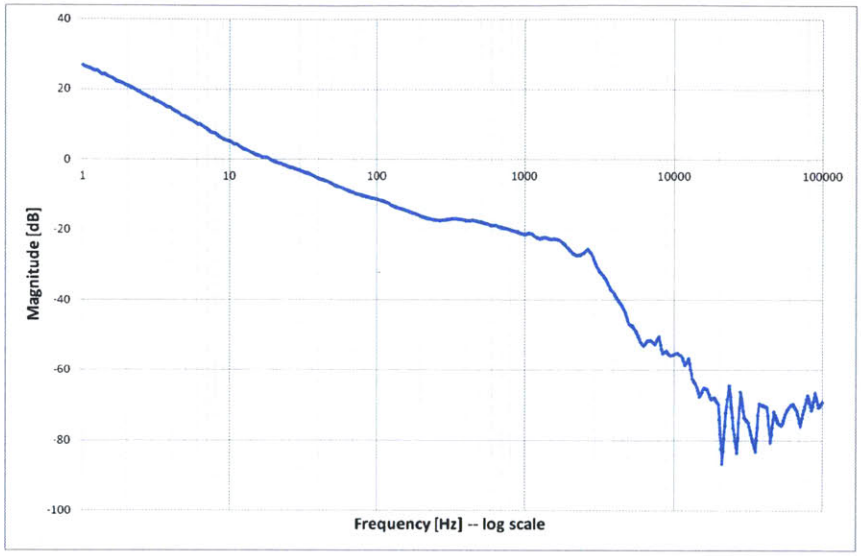

Figure 4-11: FSM300 Compensated Forward Path Bode Magnitude (f_c=19Hz)

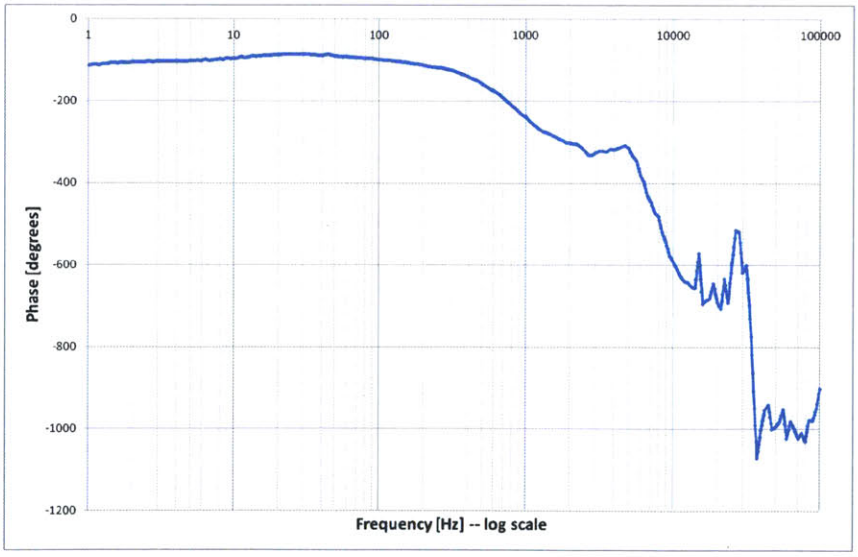

Figure 4-12: FSM300 Compensated Forward Path Bode Phase (ϕ_M=93^o)

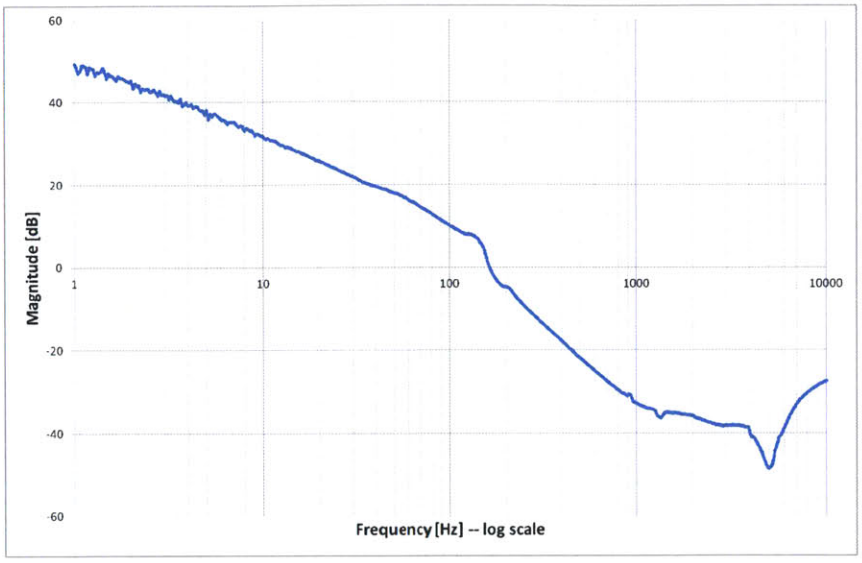

Figure 4-13: OIM101 Compensated Forward Path Bode Magnitude (f_c=162Hz)

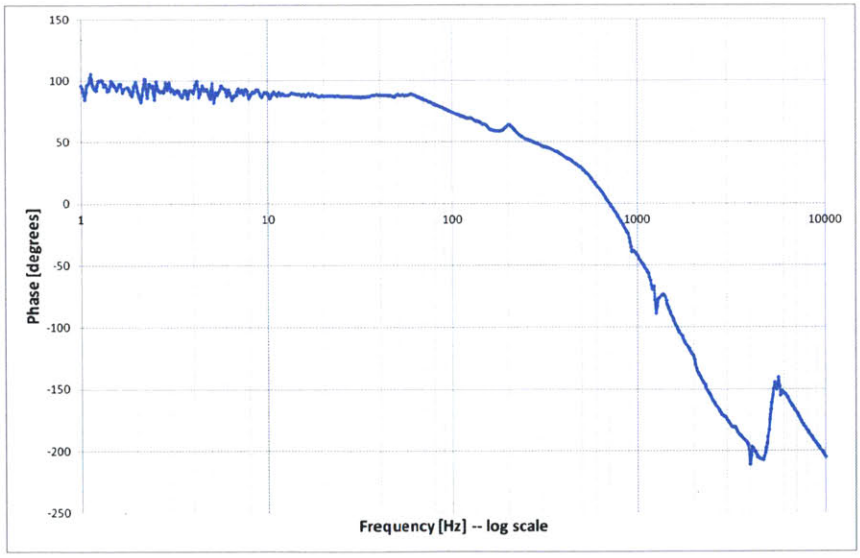

Figure 4-14: OIM101 Compensated Forward Path Bode Phase (ϕ_M=59^o)

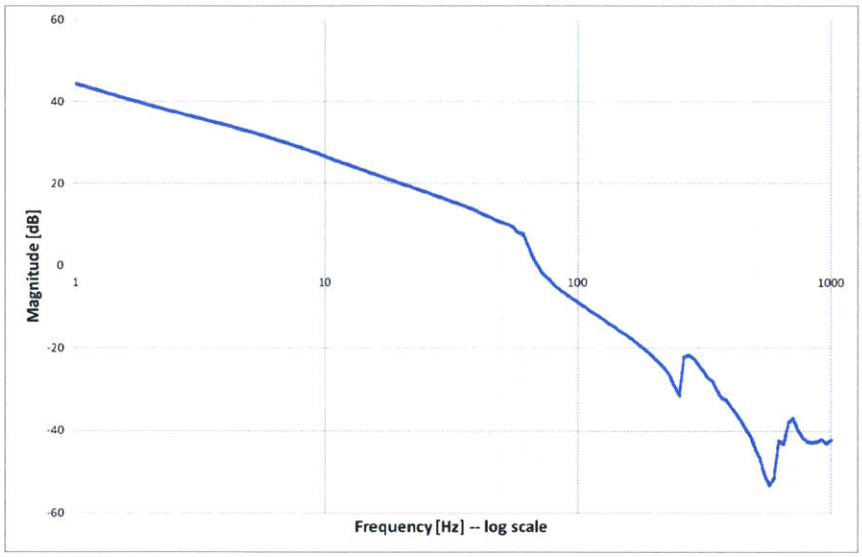

Figure 4-15: MITLL Dither Compensated Forward Path Bode Magnitude (f_c=69Hz)

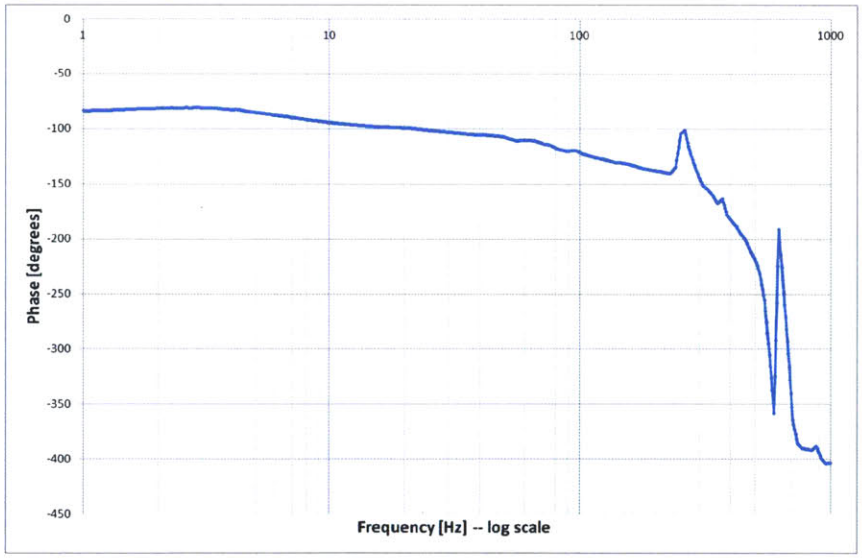

Figure 4-16: MITLL Dither Compensated Forward Path Bode Phase (ϕ_M=68^o)

4.5.2 SWaP Performance

The overall goal of designing a switching amplifier was to reduce the size, weight, and power of the FSM control circuits. The two PCBs provide a significantly smaller

and lighter form factor than the controllers shipped with the FSMs, and they easily integrate into the Group 66 benchmark system. The board uses approximately one-tenth the power that the entire FSM controller shipped with one of the mirrors uses.

4.5.3 FSM PWM Driver Board

Figures 4-17 and 4-18 show the PCB for the PWM driver circuits. The board size was designed to meet the PC-104 embedded system standard (3.55" x 3.775") and is intended to be integrated into existing PC-104 stacks in the Group 66 benchmark system. The HD-DB15 connector provides the interface to the FSM.

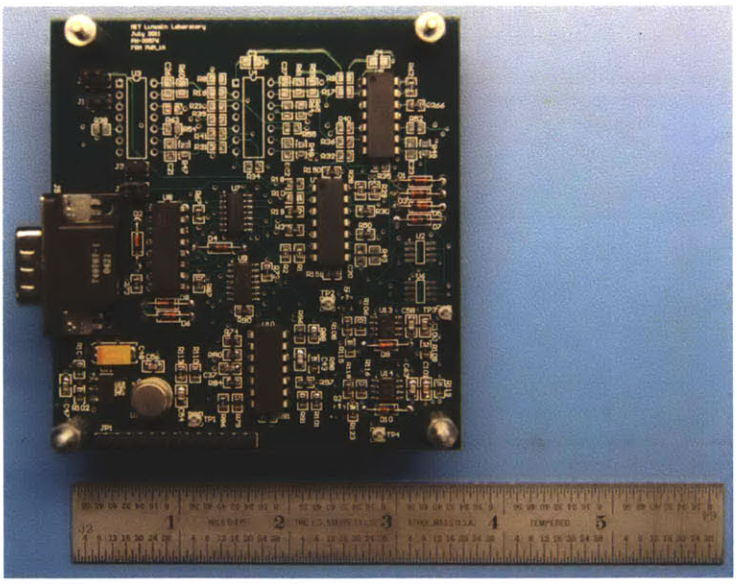

Figure 4-17: FSM PWM Driver Board [Top]

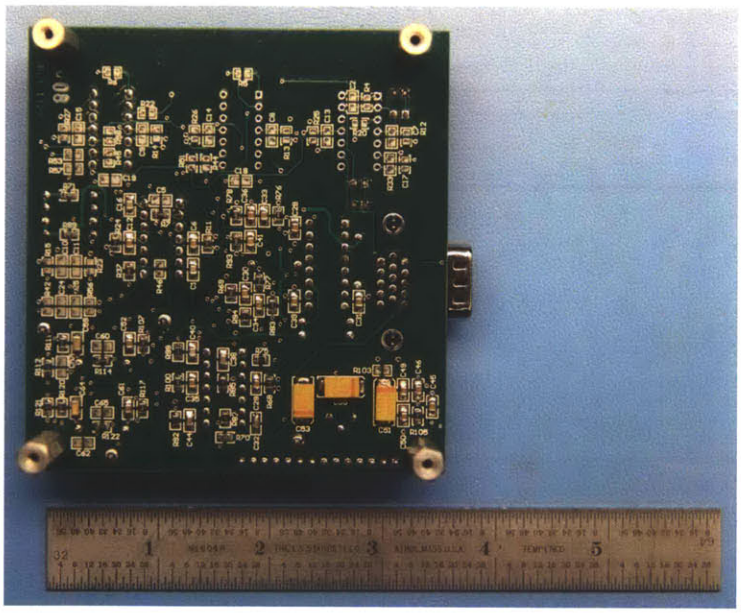

Figure 4-18: FSM PWM Driver Board [Bottom]

4.5.4 FSM Compensator Board

Figures 4-19 and 4-20 show the PCB for the minor loop and series compensator circuits, as well as the coordinate transformer. This board interfaces to the PWM board through the 14-pin header (JP1 in Figure 4-19). The compensator board size was also designed to meet the PC-104 embedded system standard (3.55" x 3.775") and is intended to be integrated into existing PC-104 stacks in the Group 66 benchmark system. The HD-DB15 connector provides the power and signal control interface to the entire FSM control loop.

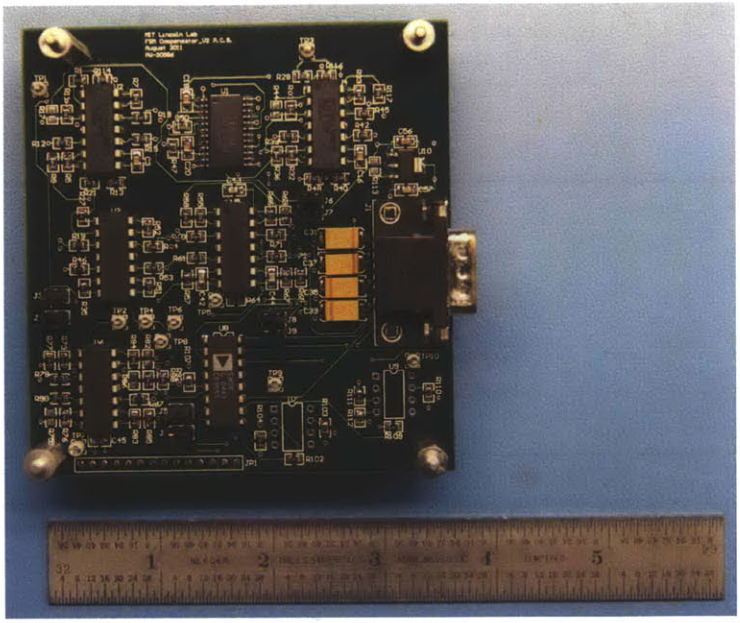

Figure 4-19: FSM Compensator Board [Top]

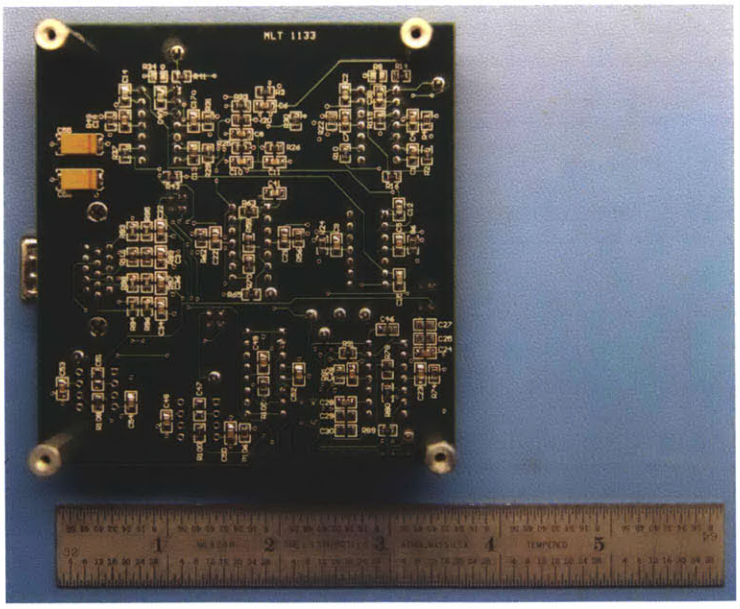

Figure 4-20: FSM Compensator Board [Bottom]

4.5.5 FSM Driver Configurations for Mirrors

Table 4.2 summarizes the key features of the load configurations for the PWM driver and compensator circuits used to control the three different FSMs previously described.

Table 4.2: Mirror Comparison: Load Configurations

	FSM300	**OIM101**	**MITLL Dither**
Switching Frequency	200kHz	150kHz	120kHz
Supply Voltage	5V	5V	7V
Lag Zero Frequency	12.45Hz	28Hz	4.7Hz
Tow-Thomas Zero Frequency	12.45Hz	28Hz	4.7Hz

Chapter 5

Tracking Sensor Investigation

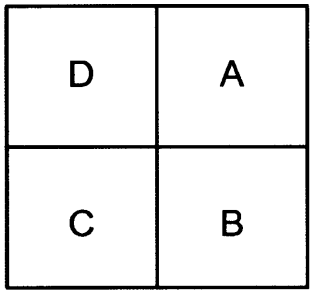

Figure 5-1: Quad Cell Square

The cost of the spatial tracker in the Group 66 benchmark system is currently dominated by the primary tracking sensor, a Focal Plane Array. FPAs are typically composed of millions of detector devices such as avalanche photo diodes (APDs) or p-intrinsic (PIN) photo diodes, where the energy represented at the output of each detector device is less than a millionth of that incident on the entire focal array. This characteristic results in a high resolution sensor which can be used for centroid tracking with reduced background sensitivity. However, a disadvantage of centroid calculations for an NxN pixel FPA is that the calculations consume valuable computation time, which limits the readout bandwidth of the sensor. This chapter investigates the use of a lower cost, lower power, and higher bandwidth tracking sensor called a quad cell. A quad cell falls into the category of quadrant detectors and is composed

of four photo diodes arranged in a 2x2 array. The received light intensity on the four photo diodes can be used to quickly calculate tracking signals, because the read-out time is small. Given the quad cell shown in Figure 5-1, two-axes Azimuth and Elevation tracking signals are calculated according to Equations 5.1 and 5.2.

$$AZ = \frac{(A+B)-(C+D)}{A+B+C+D} \tag{5.1}$$

$$EL = \frac{(A+D)-(B+C)}{A+B+C+D} \tag{5.2}$$

Where A, B, C, and D represent voltages converted from the photo currents out of the four photodiodes. Due to the smaller number of devices, quad cells provide a lower-cost alternative to the FPA tracking sensor, financially and computationally. A lateral effect sensor is a device that is nearly equivalent to the quad cell, however, it is constructed in a way to minimize the dead zones between the four photodiodes.

5.1 Quad Cell Readout

5.1.1 Transimpedance Amplifier Approach

A standard approach to the front-end readout of the quad cell photo diodes is to use four transimpedance amplifiers followed by a network of operational amplifiers to perform the (5) sums, (2) differences, and (2) divisions in the AZ-EL calculations (Equations 5.1 and 5.2). Figure 5-2 shows the AZ-EL Calc Block designed for the FSM PWM driver. It is important to maximize the transimpedance value, the resistor in the feedback path of the op amp, because the SNR of the tracking signal is set by the transimpedance stage. The transimpedance value was maximized based on the voltage supply limitations of the op amps in order to allow sufficient headroom in later stages.

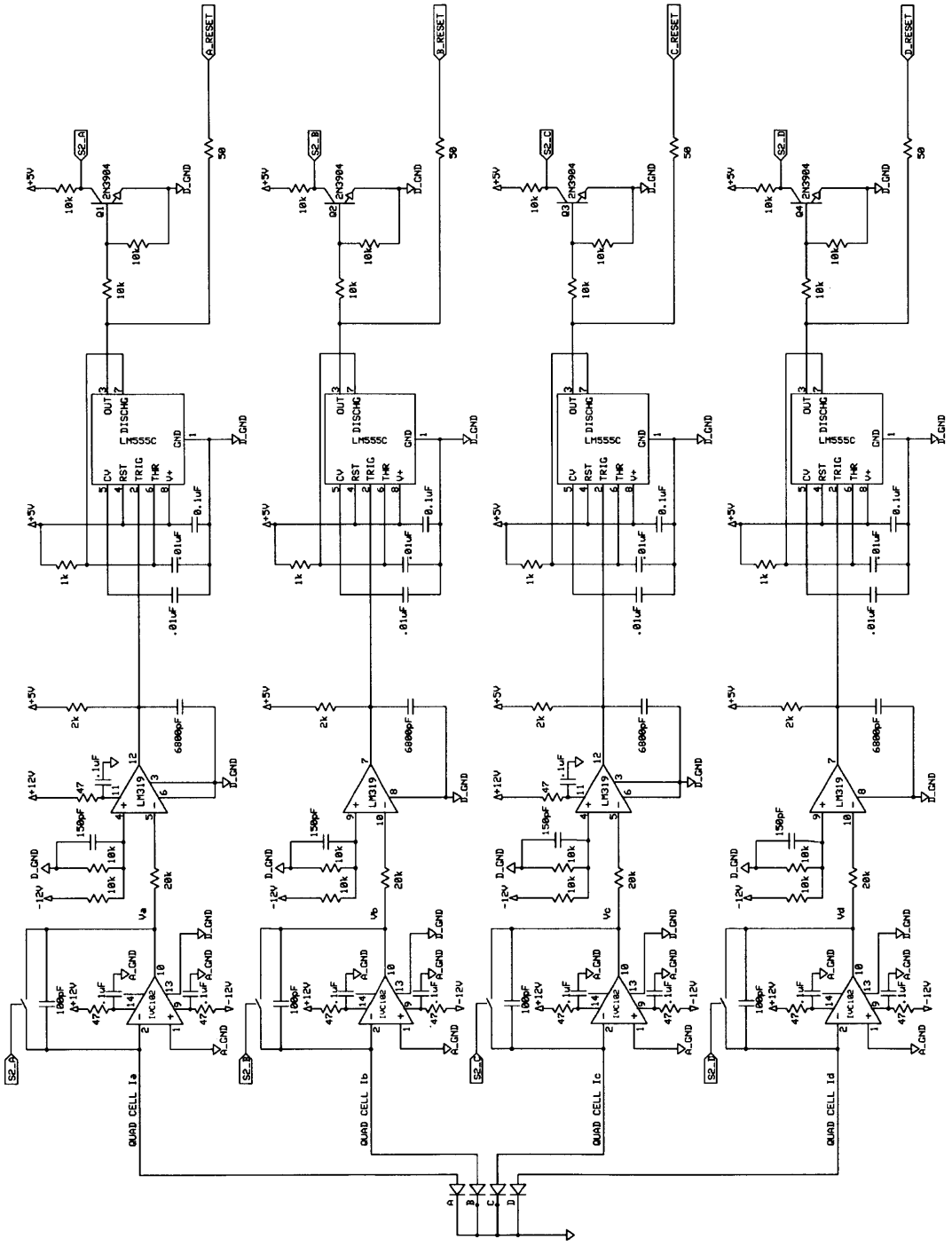

Figure 5-2: AZ-EL Calc Block

5.1.2 Integrating Digital Reset Approach

An alternative approach to the front-end readout of the quad cell photo diode's photocurrent uses charge integration and a digital reset rate. Charge accumulates on an integration capacitor, and each time the voltage across the capacitor reaches a threshold, it triggers a reset timer which generates a fixed-width digital pulse and clears the charge on the capacitor. When the optical beam is focused on one of the four quadrants, its corresponding reset rate will be higher than the other three, which integrate only error currents. Accordingly, Azimuth and Elevation tracking signals can be generated based on the reset rates of the four quadrants. The integrating digital reset circuit that was designed is shown in Figure 5-3.

5.2 Frequency-to-Voltage (F-V) Conversion

A frequency-to-voltage (F-V) converter uses a charge balancing approach that injects a precise amount of current onto an integration capacitor for a given pulse. The higher the frequency of the pulses, the more charge that will be injected, and thus, a larger output voltage. An F-V circuit is used here to take the four outputs of the integrating digital reset circuit and generate voltages. The ADVFC32 V-F and F-V Converter was selected. The part provides good linearity and operating frequency up to 500kHz. It should be noted that this approach was used only for the convenience of coupling the detector to the FSM and is not a critical component in the design of the tracking system.

5.3 Closing a Tracking Feedback Loop

5.3.1 System Tests and Performance

Using the integrating digital reset, F-V circuit, and the FSM PWM driver, a set of tracking tests were performed to demonstrate the usefulness of the quad cell sensor and efficient steering control electronics in the coarse track control loop.

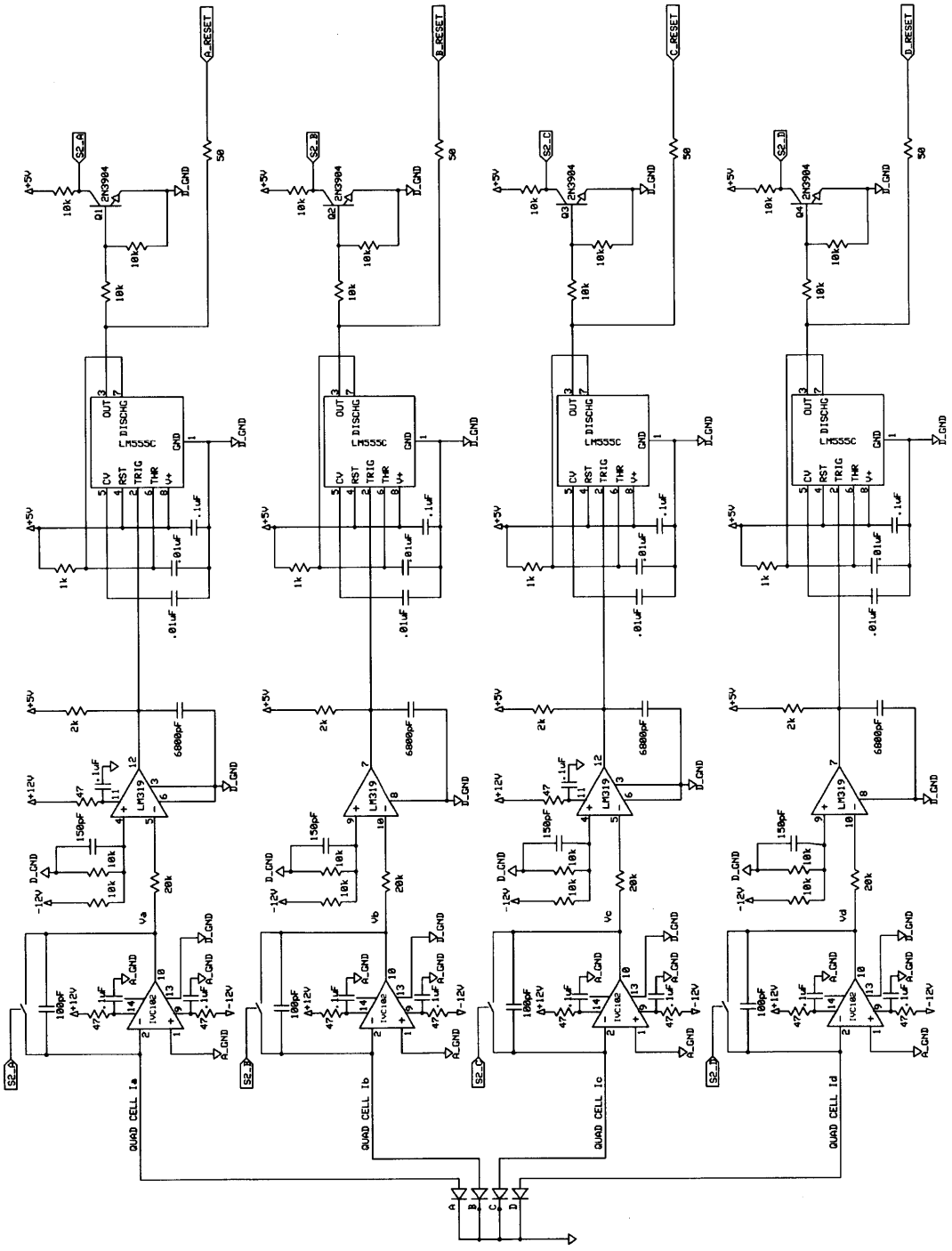

Figure 5-3: Integrating Digital Reset Circuit

5.3.2 Tracking Discriminants

A tracking discriminant can be obtained by driving a triangle wave into the AZ or EL command of an FSM driver that steers an optical beam and by observing the corresponding tracking signal output of the tracking sensor. Figures 5-4 and 5-5 show the tracking discriminant obtained from testing the quad cell sensor. The green triangle wave is the command into the FSM driver EL axis and the yellow waveform is the tracking signal EL output. The slopes of the linear parts of the two waveforms are used to derive the angle-to-voltage transfer function, or tracking sensor gain, also referred to as the slope factor (SF) in the noise equivalent angle (NEA) calculations (see appendices).

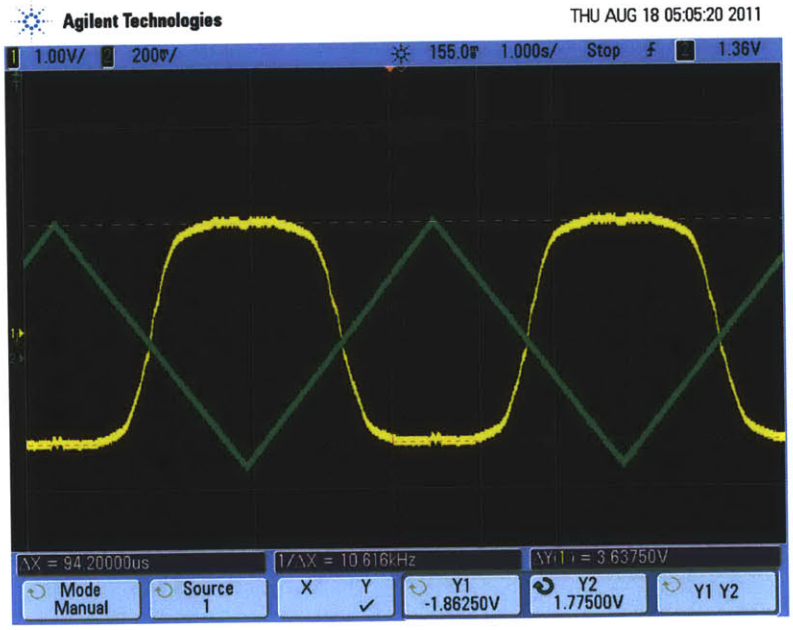

Figure 5-4: Tracking Discriminant Wide View

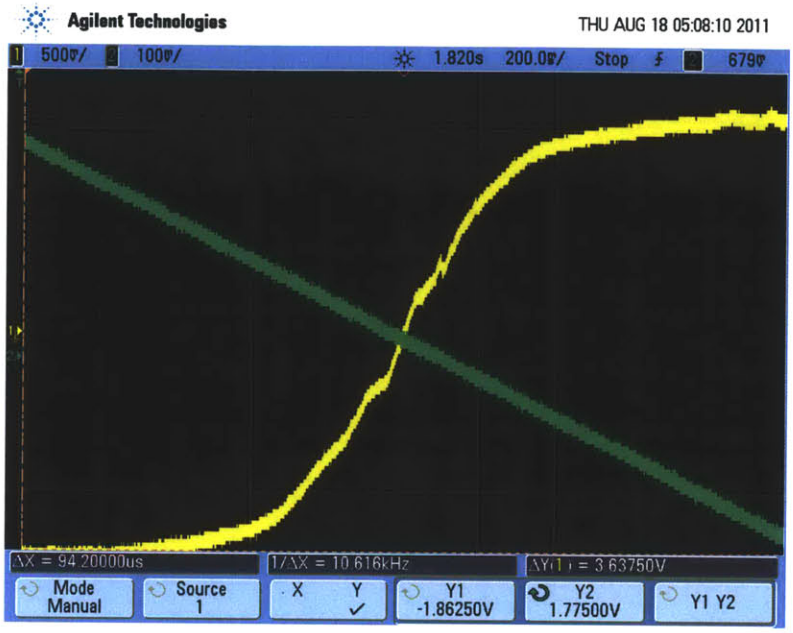

Figure 5-5: Tracking Discriminant Narrow View

The inverse SFs (voltage-to-angle transfer functions) for the AZ and EL axes are given by:

$$SF_{AZ}^{-1} = (\frac{26mrad}{10V})(\frac{\Delta V_{DRIVE}}{\Delta t_{DRIVE}})(\frac{\Delta t_{QUAD}}{\Delta V_{QUAD}})2 \tag{5.3}$$

$$SF_{EL}^{-1} = (\frac{26mrad}{10V})(\frac{\Delta V_{DRIVE}}{\Delta t_{DRIVE}})(\frac{\Delta t_{QUAD}}{\Delta V_{QUAD}})2\cos\theta \tag{5.4}$$

Where the first term comes from the FSM300 mirror used in this test and represents the angular range for a 10V command. The discriminants shown in Figures 5-4 and 5-5 were captured during tests on the EL axis. Extracting the two slopes and calculating the inverse SF:

$$SF_{EL}^{-1} = (\frac{26mrad}{10V})(\frac{0.5V}{1.6s})(\frac{0.28s}{1.5V})2\cos\frac{\pi}{4} \simeq 2.19x10^{-4}\frac{rad}{V} \tag{5.5}$$

This SF is a figure of merit for the quad cell as a tracking sensor. For a required NEA, the SF for the quad cell sets the SNR requirements according to the following

equation:

$$NEA = \frac{1}{SF\sqrt{SNR}} = \frac{219\mu rad}{\sqrt{SNR}} \tag{5.6}$$

Figure 5-6 shows how the NEA varies with the electrical SNR for tracking with this sensor.

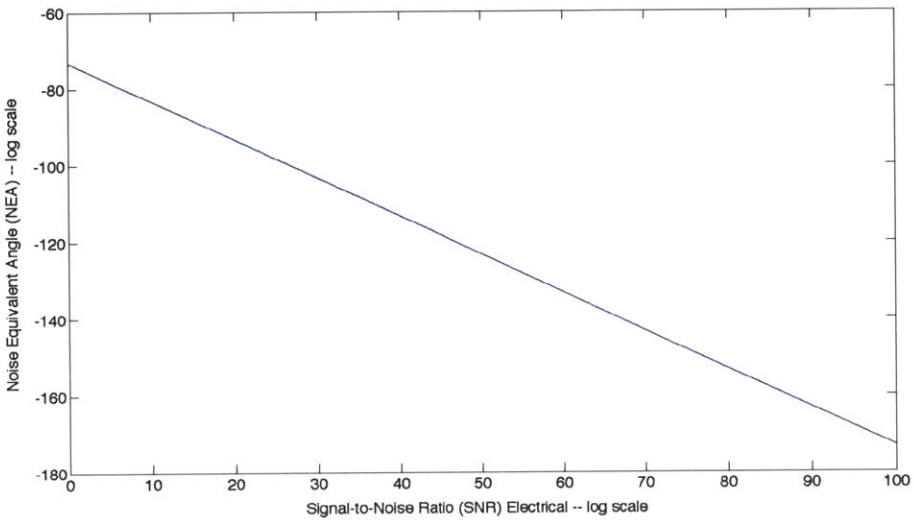

Figure 5-6: NEA vs. Electrical SNR for SF=4,566.2, Log-Log

Closer inspection of this curve shows that sub micro-radian NEA requires an SNR>46.85 dB electrical, 23.43 dB optical. The higher SNR requirement is the trade-off of using a lower cost, lower power, and higher bandwidth tracking sensor over a more expensive, higher resolution tracking sensor with a larger SF. If the system can produce sufficient SNR levels to meet the NEA requirements, the quad cell provides a number of advantages as the primary tracking sensor in the course track control loop of the MITLL spatial tracker.

Chapter 6

Flipper Motor Driver

Stepper motors are used to insert optics (i.e. filters, reflective lenses) in and out of the laser beam path. The Group 66 benchmark lasercom system has several stepper motors in the spatial tracker. The current system uses the New Focus 8892 Motorized Flipper (shown in Figures 6-1 and 6-2), which accommodates 1 inch diameter optics. Each stepper motor comes with its own hand pad that has a rocker switch to toggle the motor between its two states. The hand pads are useful in a lab setting where space is not limited and hand operation is desirable, however, in an effort to reduce size and weight for integration into the Group 66 lasercom system, a new driver circuit was designed.

6.1 Specification

The specification for the design required the following:

- Single circuit to drive the eight flipper motors on the ground terminal or the four motors on the aircraft terminal
- Reduction in size and weight of motor controls
- Removal of unnecessary functionality of the hand pad
- Individual addressing mode for four of the eight motors

- Individual and simultaneous addressing mode for four of the eight motors

- Design PCB board size to meet the PC-104 embedded system standard (3.55" x 3.775")

Figure 6-1: New Focus 8892 Flipper

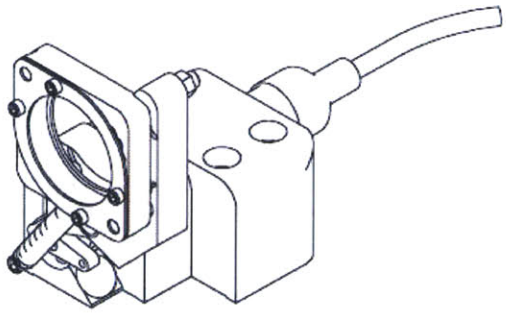

Figure 6-2: New Focus 8892 Datasheet Drawing

6.2 Driver Circuit

6.2.1 Characterization of Hand Pad

The design began with a characterization of the hand pad controls required to drive a single flipper motor. The signal required to fully transition the motor between states was measured as a 2.25s pulse of 5.5V, with correct polarity. During transition a motor consumes 300-500 mA of current.

6.2.2 Flipper Motor Driver Circuit

The block diagram in Figure 6-3 provides an overview of the Flipper Motor Driver circuit. The circuit provides bidirectional control of up to eight motors. Four of the eight motors can be operated in an individual, addressed mode. The other four motors can be operated in an individual, addressed or simultaneous flipping mode. The control interface to the circuit consists of seven control signals that drive seven TTL inputs. Three of the control lines (A, B, C) drive the address inputs of a 3-to-8 line decoder/demultiplexer and provide the ability to individually address up to eight motors. Control signals CTL_T1 and CTL_T2 are the trigger signals for the timers used in the individual, addressed flipping mode, which generate single 2.25s fixed-width pulses. Control signal CTL_T3 is the trigger signal for the timer used in the simultaneous flipping mode. Control signal CTL_T4 is the direction control signal that controls which way the motors spin in the simultaneous flipping mode. The three trigger signals are driven through inverters to provide active-high operation to the microprocessor and avoid unwanted flipper motor transitions during power cycles. The one-shot timers generate 2.25s fixed-width voltage pulses, which propagate through the logic to the line drivers where the motors are actually driven.

The circuit implementation of the block diagram is split between Figures 6-4 and 6-5 with the address line inverters not shown. The hardware interface to the circuit is a DB9 connector with seven control lines and two power supply lines (5V and GND).

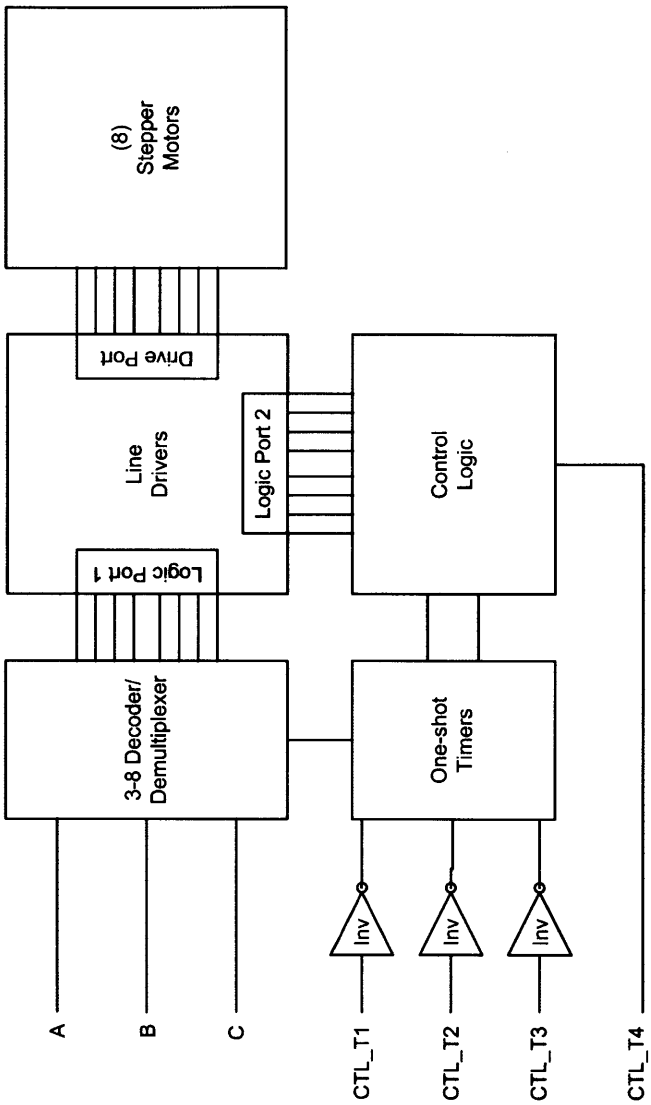

Figure 6-3: Flipper Drive Overview

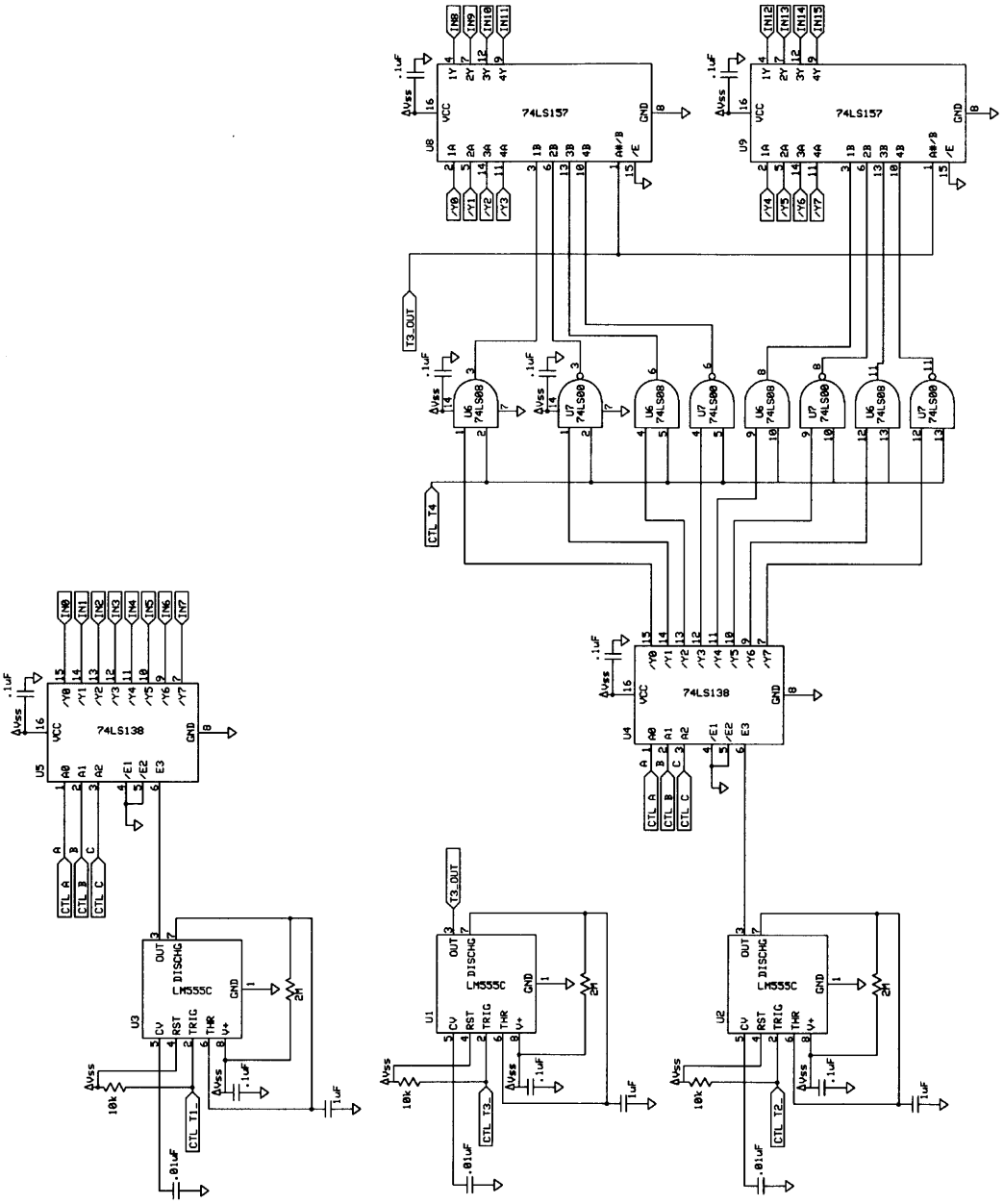

Figure 6-4: Flipper Control Logic

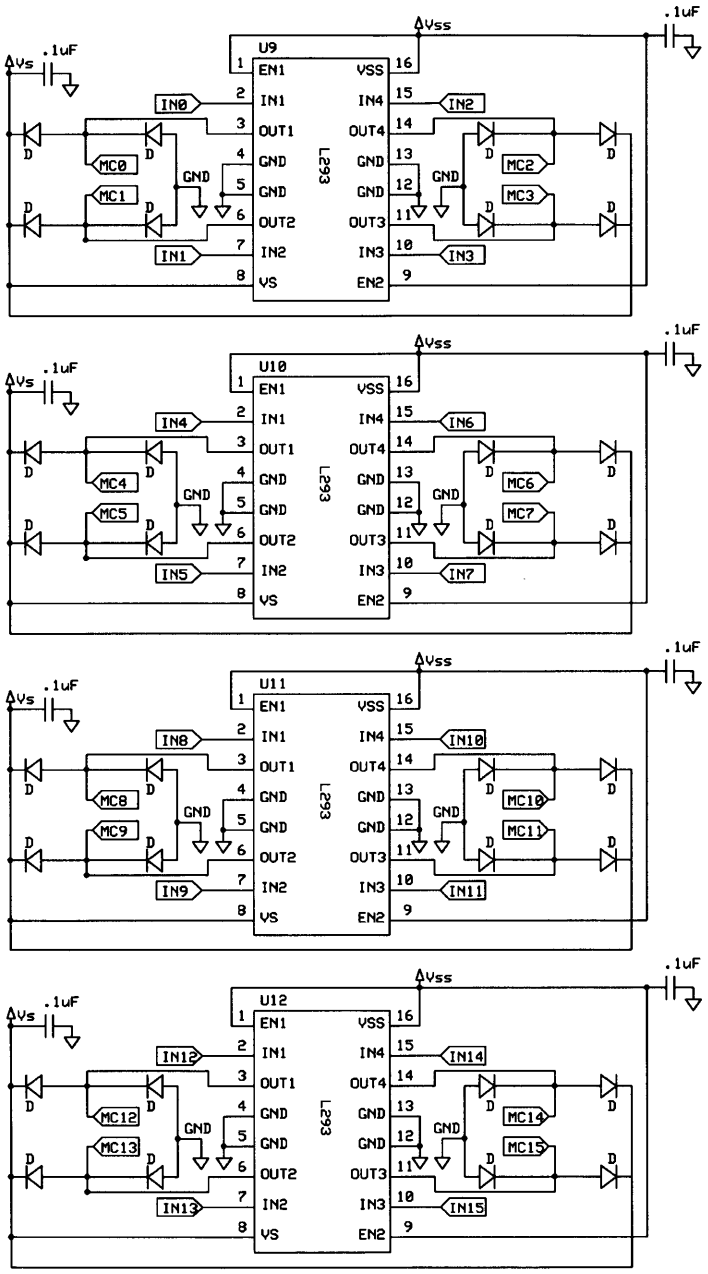

Figure 6-5: Flipper Drivers

6.3 Performance and Results

The static power dissipation is less than 1W. During the 2.25s transition, the board consumes a maximum power of 2.5W per channel.

The design was completed in August of 2010 and layed out on a PCB that was incorporated into the Group 66 October 2010 flight tests. The new driver board is smaller and lighter than the previous driver, and integrates with the benchmark system. It consumes the minimum power needed to fully transition the stepper motor.

6.3.1 Flipper Motor Driver Board

Figure 6-6 shows the PC-104 size PCB for the Flipper Motor Driver circuit in a test enclosure. Eight 3.5mm audio jack connectors for eight stepper motors are shown on the left side of the board.

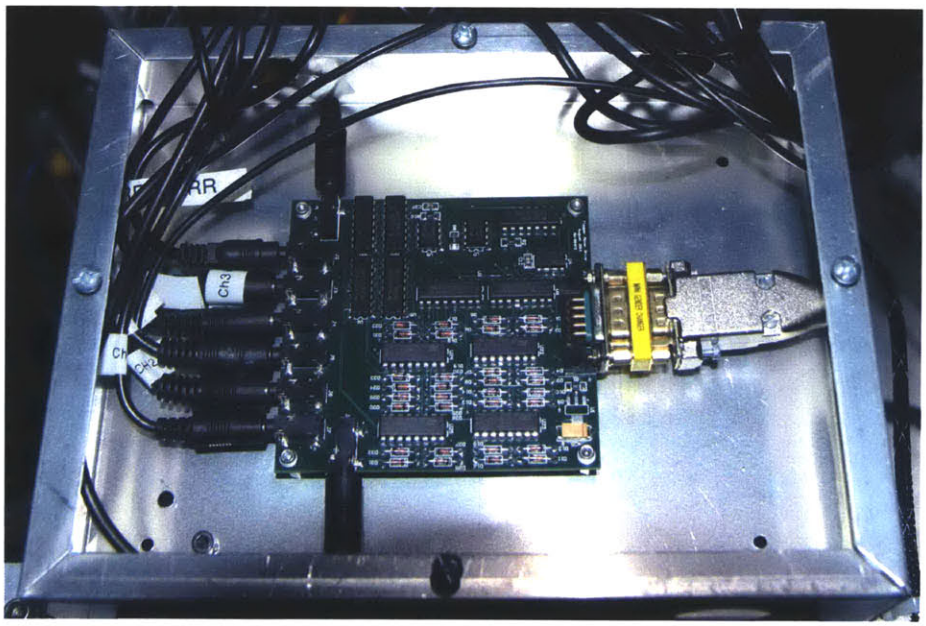

Figure 6-6: Flipper Motor Driver Board

Chapter 7

Conclusion

This thesis presented the design of circuits for a spatial tracker and improvements in size, weight, and power (SWaP) that can be made to the coarse track control loop in a benchmark lasercom system. It includes the design of an efficient PWM switching amplifier topology for controlling an FSM as well as the results of closing three compensated mirror control loops. It also includes an investigation of a lower cost, lower power, and higher bandwidth tracking sensor, and the results of closing a tracking feedback loop with a quad cell and PWM-driven FSM. Lastly, it includes a driver for controlling optical stepper motors. These contributions focused on the goal of low size, weight, and power to meet the requirements of an aircraft or space-based lasercom system.

7.1 Future Work

The results of this thesis lay groundwork in Group 66 for future development of low SWaP drivers for optical steering elements and the evaluation of new tracking sensors. One such tracking sensor that remains to be investigated is the lateral effect sensor, which is composed of a 2-by-2 array of detector devices, much like a quad cell, however it is constructed in a way that removes the large dead zones between the devices. This feature improves the linearity of the sensor in tracking applications and makes it a promising option for the primary sensor in the spatial tracker.

Appendix A

Spring-Mass-Damper Systems

This appendix contains the relevant force calculations for single-mass, single-spring and two-mass, two-spring spring-mass-damper (SMD) systems used in the model of the Fast Steering Mirror (FSM). In both cases, assume ideal masses that are unaffected by friction, ideal springs with no mass or internal damping, and a massless damper.

A single-mass, single-spring SMD system is shown in Figure A-1.

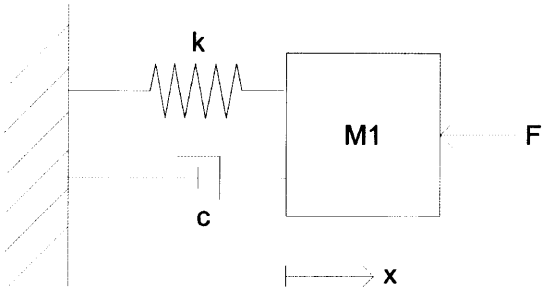

Figure A-1: Single-Mass, Spring-Mass-Damper System

Hooke's Law states that for small, non-distorting displacements, the spring provides a negative restoring force given by:

$$F_{spring} = -kx \tag{A.1}$$

The force due to the damper is proportional to the velocity of the mass and is

given by:

$$F_{damp} = -c\dot{x} \tag{A.2}$$

The superposition of forces yields:

$$\sum F = M_1\ddot{x} = -kx + -c\dot{x} \tag{A.3}$$

The result is a second-order differential equation, given by:

$$\ddot{x} + \frac{c}{M_1}\dot{x} + \frac{k}{M_1}x = 0 \tag{A.4}$$

The natural frequency of the second-order system is given by:

$$\omega_o = \sqrt{\frac{k}{M_1}} \tag{A.5}$$

And the damping of the second-order system is given by:

$$\zeta = \frac{1}{2}\frac{c}{\sqrt{M_1 k}} \tag{A.6}$$

For a two-mass, two-spring SMD system as shown in Figure A-2, a similar analysis can be performed.

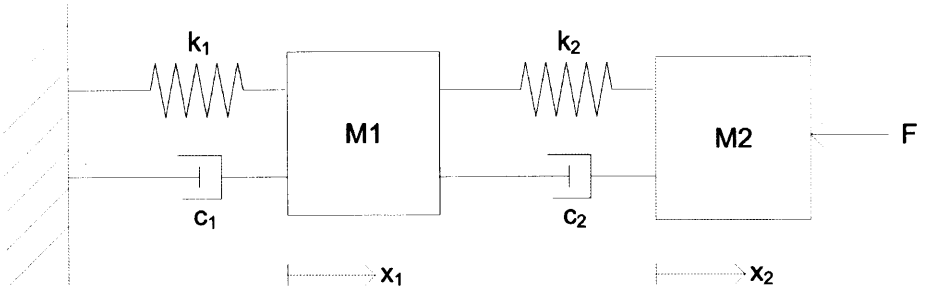

Figure A-2: Two-Mass, Spring-Mass-Damper System

The superposition of forces on each mass yields two differential equations:

$$M_1\ddot{x_1} = -k_1x_1 + -c_1\dot{x_1} + k_2(x_2 - x_1) + c_2(\dot{x_2} - \dot{x_1}) \tag{A.7}$$

$$M_2\ddot{x_2} = -k_2(x_2 - x_1) - c_2(\dot{x_2} - \dot{x_1}) \tag{A.8}$$

If $M_1>>M_2$, this system will have two major resonances. A primary mechanical resonance results from the under damped energy transfer between the spring and the inertia of the mass. A secondary resonance results due to mechanical decoupling that occurs when parts of the mirror depart from a rigid body approximation. The mass M_2 represents the part of the mirror that decouples from the main mass, M_1. The natural frequencies of these two resonances are given by:

$$\omega_{primary} = \sqrt{\frac{k_1}{M_1 + M_2}} \tag{A.9}$$

$$\omega_{secondary} = \sqrt{\frac{k_2}{M_2}} \tag{A.10}$$

The damping ratios are given by:

$$\zeta_{primary} = \frac{1}{2}\frac{c_1}{\sqrt{(M_1 + M_2)k_1}} \tag{A.11}$$

$$\zeta_{secondary} = \frac{1}{2}\frac{c_2}{\sqrt{M_2k_2}} \tag{A.12}$$

Appendix B

Measuring Inductance

One must often measure the impedance characteristics of a real inductive load to determine parasitic element values. A good model for a real inductor is shown below in Figure B-1. In addition to the ideal inductance, there is a parasitic DC series resistance (R_{series}) due to the wire resistance and a parasitic parallel capacitance ($C_{interwinding}$) due to the interwinding capacitance.

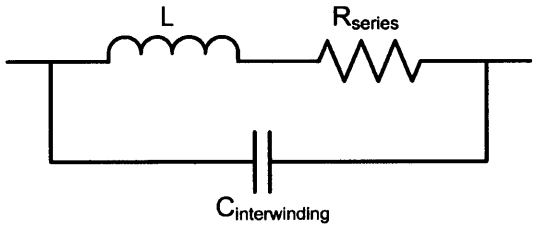

Figure B-1: Real Inductor Model

The the impedance characteristic of a real inductor with values L=50μH, R_{series}=1Ω, and $C_{interwinding}$=1pF was simulated in MATLAB and is shown in Figure B-2. The parasitic resistance introduces a 1Ω offset in the curve that dominates at low frequencies, while the parasitic capacitance introduces a component resonance at 22.5MHz. The region in between is where the inductor looks inductive, up to the resonance, after which it look capacitive.

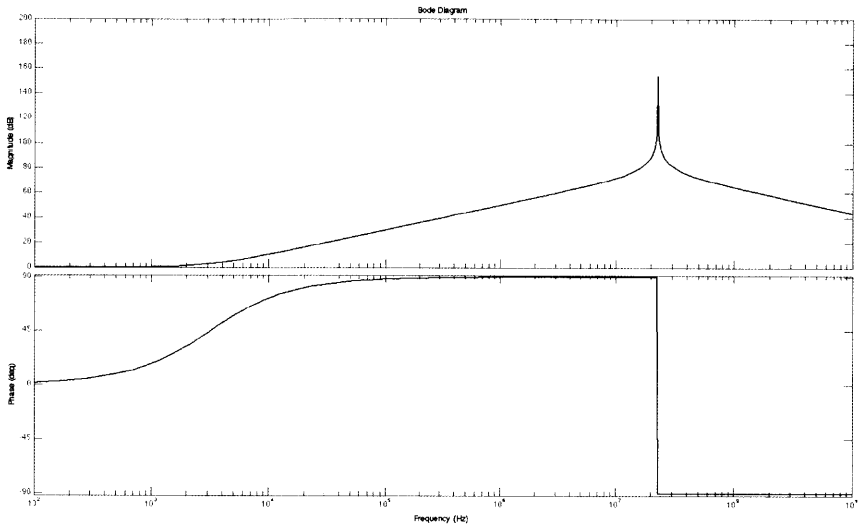

Figure B-2: Real Inductor Impedance Bode Plots

The DC resistance of the inductor is easily measured with a multimeter. The inductance and interwinding capacitance can both be measured using a precision resistor, signal generator, and oscilloscope. The precision resistor (R_{prec}) is placed in series with inductor under test and the series load is driven with the signal generator. It is assumed that the signal generator is not driven close to the component resonance and the real inductor can be approximated as having only a parasitic resistance. Observing the voltage (V_O) at the impedance divider between the precision resistor and the inductor, the divider relation is given by:

$$\frac{V_O}{V_{SIG}} = \frac{R_{series} + j\omega L}{R_{prec} + R_{series} + j\omega L} \tag{B.1}$$

The magnitude of the impedance is easily observed on the oscilloscope and given by:

$$\left|\frac{V_O}{V_{SIG}}\right| = \frac{\sqrt{(R_{series})^2 + (\omega L)^2}}{\sqrt{(R_{prec} + R_{series})^2 + (\omega L)^2}} \tag{B.2}$$

The frequency is swept and the half-power point is measured on the oscilloscope.

The half-power point occurs at the frequency when the voltage falls to $\frac{1}{\sqrt{2}}$ the low frequency value.

$$|\frac{V_O}{V_{SIG}}| = \frac{\sqrt{(R_{series})^2 + (\omega L)^2}}{\sqrt{(R_{prec} + R_{series})^2 + (\omega L)^2}} = \frac{1}{\sqrt{2}} \tag{B.3}$$

$$\frac{(R_{series})^2 + (\omega L)^2}{(R_{prec} + R_{series})^2 + (\omega L)^2} = \frac{1}{2} \tag{B.4}$$

$$L = \frac{\sqrt{(R_{prec} + R_{series})^2 - 2R_{series}^2}}{2\pi f} \tag{B.5}$$

Appendix C

Noise Equivalent Angle (NEA) Calculations for Quadrant Detector Device[1]

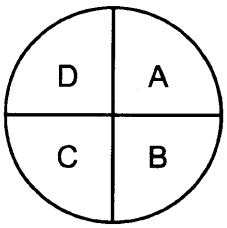

For the quad cell shown above, where A, B, C, and D represent voltages converted from the currents out of four photodiodes, the ideal Azimuth (AZ) and Elevation (EL) tracking signals are calculated as the following:

$$AZ = \frac{(A+B)-(C+D)}{A+B+C+D} \tag{C.1}$$

$$EL = \frac{(A+D)-(B+C)}{A+B+C+D} \tag{C.2}$$

If there is noise in the transimpedance (current-to-voltage) stage that converts the diode photo currents to the voltages A, B, C, and D, the tracking signals can be

rewritten to include noise terms:

$$AZ_n = \frac{A + n_a + B + n_b - C - n_c - D - n_d}{A + B + C + D + n_a + n_b + n_c + n_d} \tag{C.3}$$

$$EL_n = \frac{A + n_a + D + n_d - B - n_b - C - n_c}{A + B + C + D + n_a + n_b + n_c + n_d} \tag{C.4}$$

For large SNR levels, the noisy tracking signals can be arranged as a superposition of the ideal term and the normalized noise term:

$$AZ_n = \frac{A + B - C - D}{A + B + C + D} + \frac{n_a + n_b - n_c - n_d}{A + B + C + D} \tag{C.5}$$

$$EL_n = \frac{A + D - B - C}{A + B + C + D} + \frac{n_a + n_d - n_b - n_c}{A + B + C + D} \tag{C.6}$$

If the noise terms are defined by a zero mean process, the expected values of the noisy tracking signals are:

$$E[AZ_n] = \frac{A + B - C - D}{A + B + C + D} \tag{C.7}$$

$$E[EL_n] = \frac{A + D - B - C}{A + B + C + D} \tag{C.8}$$

The statistical variance of the noisy tracking signals is defined by:

$$\sigma_{AZ}^2 = E[AZ^2] - E[AZ]^2 \tag{C.9}$$

$$\sigma_{EL}^2 = E[EL^2] - E[EL]^2 \tag{C.10}$$

which can be rewritten as:

$$\sigma_{AZ}^2 = E[AZ^2] + \frac{\sigma_a^2 + \sigma_b^2 + \sigma_c^2 + \sigma_d^2}{A+B+C+D} - E[AZ^2] = \frac{E[n_a^2] + E[n_b^2] + E[n_c^2] + E[n_d^2]}{A+B+C+D} \tag{C.11}$$

But since the noise process is zero mean, the expected values of the noise terms are equal to their variances, which simplifies the expression:

$$\sigma_{AZ}^2 = \frac{\sigma_a^2 + \sigma_b^2 + \sigma_c^2 + \sigma_d^2}{A+B+C+D} \tag{C.12}$$

And since the variances result from the same process, they are equal, which simplifies the expression further:

$$\sigma_{AZ}^2 = \frac{4\sigma_n^2}{(A+B+C+D)^2} \tag{C.13}$$

Therefore, the rms terms are:

$$\sigma_{AZ} = \frac{2\sigma_n}{A+B+C+D} \tag{C.14}$$

$$\sigma_{EL} = \frac{2\sigma_n}{A+B+C+D} \tag{C.15}$$

which can be defined in terms of the SNR:

$$\sigma_{rms} = \frac{1}{\sqrt{SNR}} \tag{C.16}$$

Lastly, to convert this to angular coordinates, multiply by the voltage-to-angle transfer function, referred to here as $\frac{1}{SF}$:

$$\sigma_{rms} = \frac{1}{SF\sqrt{SNR}} \tag{C.17}$$

This final term is referred to as the Noise Equivalent Angle (NEA), and the angle-to-voltage transfer function (SF) is referred to as the tracking sensor gain or slope factor. For a given SNR in the receiver, the tracking discriminant determines the NEA.

Bibliography

[1] Stephen G. Lambert, William L. Casey, *Laser Communication in Space.* Norwood, Massachusetts, 1st Edition, 1995.

[2] James K. Roberge, *Operational Amplifiers: Theory and Practice.* New York, New York, 1st Edition, 1975.

[3] Christopher Bowick, John Blyler, Cheryl Ajluni, *RF Circuit Design.* Boston, Massachusetts, 2nd Edition, 2007.

[4] Kent Lundberg, *Feedback Systems for Analog Circuit Design.* Unpublished, 2006.

[5] Kent Lundberg, *Become One with The Transistor.* Unpublished, 2006.

[6] Norman S. Nise, *Control System Engineering.* Hoboken, New Jersey, 5th Edition, 2005.

[7] Paul Horrowitz, Winfield Hill, *The Art of Electronics.* New York, New York, 2nd Edition, 1989.

[8] John G. Kassakian, Martin F. Schlecht, George C. Verghese, *Principles of Power Electronics.* Reading, Massachusetts, 1st Edition, 1991.

[9] Murphy, Vocipelli, Wilcox, Crucioli, Williams, *A Conical Scan Free Space Optical Tracking System for Fading Channels.* Lexington, Massachusetts, 2009.

[10] C. Henry Edwards, David E. Penney, *Elementary Differential Equations.* Upper Saddle River, New Jersey, 6th Edition, 2008.

[11] Taylor Barton, *6.331 Advanced Circuit Techniques: Power Conversion Lecture 2.* Unpublished, 2012.